A discriminatory diagram of massive vs stratified deposits based on the sedimentation and bedload transportation rates. Experimental investigation and application to pyroclastic density currents.

P. Dellino[1*], F. Dioguardi[2], D.M. Doronzo[3] and D. Mele[1]

[1] Dipartimento di Scienze della Terra e Geoambientali, Università di Bari, Italy; [2] British Geological Survey, The Lyell Centre, Edinburgh, United Kingdom; [3] Institute of Earth Sciences ''Jaume Almera", ICTJA, CSIC, Group of Volcanology, SIMGEO UB-CSIC, Lluis Sole i Sabaris s/n, 08028 Barcelona, Spain.

Abstract

Dense gas-particle jets similar to collapsing eruption columns were generated by large-scale experiments. The column collapse resulted in a ground-hugging current forming layers with bedding similar to natural pyroclastic density current deposits. At the impact of the column on the ground, a thick, massive bed was formed due to a high sedimentation rate. The flow expanded laterally into a fully turbulent, dilute gas-particle current that deposited thin layers showing ripple-like structures. The ripples were interpreted as tractional structures formed by the current ability to move bedload material settled from suspension.

Experiments fed with fine ash formed deposits without tractional structures, because fine particles require a large tangential stress to be sheared.

Experimental outcomes show that massive beds are formed where the sedimentation rate per unit width S_{rw} exceeds the bedload transportation rate Q_b by 100 times. A lower ratio generates traction at the base of the flow and formation of shear structures that increase in wavelength and height with a decreasing flux.

We present a diagram that provides a useful addition for facies analysis of pyroclastic density currents, provided that deposits representing sustained sedimentation can be identified in the field. In the diagram a decrease in the S_{rw}/Q_b ratio corresponds to an increase of bedform scale. Application of the diagram for hazard assessment purposes allow the reconstruction of the mass eruption rate of the Agnano-Monte Spina eruption at Campi Flegrei and of the Bingham rheology of the massive underflow of the Mercato pyroclastic density current at Vesuvius.

1. Introduction

1.1 General context of pyroclastic density currents

Pyroclastic density currents often form from the collapse of a dense gas-particle jet, called eruption column. They are fast moving highly hazardous flows associated with medium to large magnitude explosive volcanic eruptions. The likelihood of their formation and the nature of formative flows is strongly controlled by the flow rate at the volcanic vent,

$\rho_{mix} V_0 A$ (1)

which is called the Mass Eruption Rate, *MER*, where

$\rho_{mix} = \rho_s C + \rho_g (1-C)$ (2)

is the gas-particle mixture density, with ρ_s particle density, ρ_g gas density and C particle volumetric concentration. V_0 is vent exit velocity and A is the vent cross-sectional area of radius r (for symbols refer to the Symbol List). Typical values of *MER* for the formation of substantial pyroclastic density currents are in the range 10^7- 10^9 kgs^{-1}(Cioni et al., 2000) with V_0 in the range of 100 m/s, r in the range of 100 m, C a few percent and a specific mass flow rate per unit area at conduit exit in the range 10^3-10^4 $kgm^{-2}s^{-1}$. It has been demonstrated (Dellino et al., 2014) that the condition for the formation of a completely collapsing column is met when the densimetric Froude number at the vent, Fr'_0, is between 1 and 3, where

$$Fr'_0 = \frac{V_0}{\sqrt{g' r_0}} \quad (3)$$

with $g' = g\left(\frac{\rho_{mix} - \rho_{atm}}{\rho_{atm}}\right)$ and ρ_{atm} atmosphere density. When a complete collapse happens (i.e. no contemporaneous ash convective dispersal in the surrounding atmosphere occurs) the column is characterized by a very low, or null entrainment of atmosphere air (Dellino et al. 2014) and the eruptive mixture, along the ascending-descending trajectory, conserves its bulk density and respects Bernoulli's equation of the conservation of total pressure, with maximum height $H=V_0^2/2g$. It means that at collapse, the flow hits the ground at the same speed and particle volumetric concentration of conduit exit. The flow, after the impact, moves down the volcano flank due to the higher density of

the gas-particle mixture with respect to the surrounding atmosphere. The resulting deposits show a wide range of structures, including both massive beds and stratified layers with tractional structures like dunes and ripples (e.g., Pritchard and Gladstone, 2009). Since the last half of the last century a debate goes on whether there is a rigid demarcation between dense and dilute currents (e.g., Dade, Fisher, 1979; 2003; Sparks, R.S.J., 1976; Sulpizio et al., 2014) forming, separately, massive or stratified deposits, or there is the possibility that a flow could form both deposit types as a function of changes in the regime of sedimentation (e.g., Branney and Kokelaar, 2002; Sumner et al., 2008; Sulpizio et al., 2007, 2014). The subject is relevant for hazard assessment, because dense and dilute currents have a different impact potential. The impact of pyroclastic density currents on infrastructures and life depends on flow characteristics such as particle volumetric concentration, grain-size distribution and flow speed, in addition to temperature (Valentine, 1998; Baxter et al., 2005; Dellino et al. 2008; Manville et al., 2009; Caricchi et al., 2014; Mele et al. 2015; Esposti Ongaro et al., 2016). Metric thick, dense, massive flows are valley ponded, tend to move slowly on steep slopes, maintain high temperature and are destructive at the valley apron at the base of the volcanic edifice. Hundreds of meters thick, turbulent currents, move on the plain areas surrounding the volcano. They are able to surmount substantial topographies and are lethal also in distal reaches, because of their content of harmful fine ash taken into suspension by fluid turbulence (Druitt and Kokelaar, 2002).

1.2 Physical properties and sedimentation regimes of turbulent suspension currents

Sediment-laden flows governed by fluid turbulence, i.e. fluvial, aeolian, turbiditic and pyroclastic density currents, can transport solid particles in three main modes: suspension load, bedload and wash load. Suspension refers to particles that are sustained by turbulence and settle when their terminal velocity w_t is higher than the current shear velocity, u_*.

$$w_t = \sqrt{\frac{4Dg(\rho_s - \rho_{mix})}{3C_d\rho_{mix}}} \quad (4)$$

where D is particle size, g is gravitational acceleration, C_d is particle drag coefficient.

Bedload includes particles moved on the ground by shear stress from the overlying current. Wash load is made of particles so fine that are intimately coupled to fluid turbulence, are carried by the current and settle during the waning stage of flowage (e.g., Gladstone et al., 1998; Duller et al., 2008; Chanson, 2009; Meiburg and Kneller, 2010; Kok et al., 2012; Dellino et al., 2019).

In the time-space evolution of a current, when the settling velocity approaches flow shear velocity, particles, after being transported in suspension, eventually settle to the ground and form the bedload material (Branney and Kokelaar, 2002; Sulpizio and Dellino, 2008; Roche et al., 2013; Sulpizio et al., 2014; Lube et al., 2015; Dufek, 2016).

The bedload transportation rate is expressed, in volumetric form (Wilcock and Crowe, 2003), in terms of

$$W_i^* = \frac{(\rho_s/\rho_{fmix} - 1)gq_{bi}}{\phi_i u_*^3} \quad (5)$$

where W_i^* is a non-dimensional factor, which is a function of the shear stress at the base of the current, q_{bi} is the volumetric bedload transport rate of the i_{th} size fraction per unit width of the flow, ϕ_i the proportion of the i_{th} size fraction of the bedload and u_* is the flow shear velocity. $Q_b = \sum_i^n q_{bi}$ is the bedload transportation rate of all size fractions.

Sedimentation can be sustained as long as the flow is fed with particles (Brown and Branney, 2013; Rowley et al., 2014; Roche, 2015). The sedimentation rate $S_r = \sum_{i=1}^{n} S_{ri}$ expresses the rate of particles sedimented over a unit surface of the ground per unit time, where

$$S_{ri} = w_{ti}\rho_{si}\gamma_i \quad (6)$$

with γ_t the proportion of particles of the i_{th} size fraction (out of the total concentration) that are sedimented from the current (Dellino et al. 2019).

$$A_r = \frac{S_r}{\rho_{dep}} \quad (7)$$

is the aggradation rate of deposit thickenss d, with a bulk deposit density ρ_{dep}.

106 The time of deposit aggradation

107 $t = \frac{d}{A_r}$ (8)

108 represents the time spent by the current to form the whole deposit.

109 In some cases, it has been demonstrated that thick, massive, deposits are formed directly from
110 suspension, because of a high sedimentation rate, also called suspended-load fallout rate, which
111 inhibits traction at the bedload (Lowe, 1982 and 1988; Fisher, 1990; Druitt, 1992; Kneller and
112 Branney, 1995; Woods et al., 2002; Postma et al., 2009).

113 The hypothesis of this paper is that the limit between the formation of massive and stratified deposits
114 is governed by a threshold ratio between the sedimentation and the bedload transportation rates, and
115 is also a function of the amount of cohesive material and particle volumetric concentration (Sumner
116 et al, 2008; Baas et al., 2011). In order to verify this hypothesis, the sedimentation and bedload
117 transportation rates need to be measured in actual currents. Unfortunately, it is difficult to monitor
118 the formation of deposit structures directly during an eruption. In fact, pyroclastic density currents
119 are hard to predict and/or to instrument, and the measurement of their internal characteristics, as of
120 today, is impossible from remote sensing. In the present paper, the sedimentation and bedload
121 transportation rates are measured in currents formed by means of large-scale experiments that were
122 designed as to simulate pyroclastic density currents formed by the collapse of an eruption column.
123 As an outcome of experiments, a diagram for discriminating between massive and stratified deposits
124 is proposed. In the diagram, the scale of bedforms of stratified deposits increases where the ratio
125 between sedimentation and bedload sedimentation rates decreses. The diagram is applied to deposits
126 of Vesuvius and Campi Flegrei volcanoes in Southern Italy, as to verify its utility in the reconstruction
127 of the physical characteristics of past eruptions of the two hazardous Italian active volcanoes.

128

129 **2. Experimental setup, materials and methods**

130 Experiments were carried out with the aim of generating density currents forming measurable
131 massive and stratified deposits, starting from a dense gas-particle jet similar to a collapsing eruption

column. The experiments consider the case of a completely collapsing eruption column and do not include all the possible variations as, for example, the occurrence of contemporaneous fallout, re-fragmentation of particles after conduit exit, or the effect of valleys and/or topographic barriers.

On previous papers (Dellino et al., 2011; Dellino et al., 2014) experiments carried out both at ambient temperature and up to 300° C demonstrated that, in the case of completely collapsing columns (in contrast with convective plumes), temperature doesn't play a major role neither in determining the jet dynamics nor in the sedimentation from the base of the ground-moving density current. In the present paper, experiments carried out at ambient temperatures are considered.

The experiments were performed with the apparatus described in detail by Dellino et al., 2007; 2010a; 2010b; and 2014. The design (Fig. 1) consists of pressurized-gas bottles (Fig. 1a) connected, via valves and manometers, to long hoses that are charged with a known amount of gas (nitrogen) at known pressure. In this way, a known quantity of potential energy is stored, and is released by gas expansion upon opening the valves. The hoses are connected to a hub of fast solenoid valves (Fig. 1b) that are attached, via short hoses and blow nozzles, to the base plate of a 3.2 m long, vertical cylindrical conduit with 0.6 m internal diameter (Fig. 1c). The blow nozzles allowed the injection of gas into the conduit and its coupling to the particulate material resting on the base plate.

The particulate material used in the experiments comes from pyroclastic deposits of the Mercato eruption at Vesuvius and of the Agnano Monte Spina eruption at Campi Flegrei in Southern Italy. The grain size of two compositions, representing the coarse (from Vesuvius) and fine (from Campi Flegrei) end members, are plot on Fig. 2 as to show the range used. The coarser composition ranges from lapilli to fine ash (a few micrometres to a few centimetres, Fig. 2a), with a median size D_{sm} = 0.75 mm. It is made of dense lithic, vesicular glass and crystal components. The fine composition (Fig. 2b) has median size D_{sm} = 0.066 mm and is made almost exclusively of glass fragments.

In this paper, five runs are considered. For each run data were collected at multiple locations along flow runout. The particle load (up to 350 kg), gas pressure and grain size were varied among runs as to obtain density currents of different speed, particle concentration and granulometry (see Tab.1).

158 Blue plastic sheets were mounted on the ground, over an ample area around the conduit (about 2000
159 m^2), so to allow easy sampling of the deposits left after the experiments. The deposits were
160 photographed and sampled over the whole dispersal area. The mass of sediment per unit area was
161 calculated by sampling the sediment over a rectangular area, at regular distances (Fig. 3), and
162 weighting it. The deposits were analysed in the laboratory for grain-size characterization and
163 componentry analysis. Grain size analysis was carried on by dry sieving for the fractions > 0.125
164 mm and by means of a Coulter Multisizer IV for the fractions ≤ 0.125 mm. Data were combined by
165 software as histograms at half-phi interval.
166 The experiments start with the computer-controlled opening of the solenoid valves, allowing a fast
167 coupling of the pressurized gas with the pyroclastic material filling the conduit that, on mixing with
168 the expanding gas, accelerates along the conduit (Dioguardi et al., 2013). The two-phase mixture is
169 finally expelled out of the conduit in the form of a dense gas-particle jet. The jet, with conduit exit
170 velocities up to 20 m/s, reaches a maximum height (typically more than 10 m over conduit exit, Fig.
171 4a), which follows the prescription of Bernoulli's equation. Along the ascending-descending
172 trajectory no significant air entrainment occurs (Dellino et al., 2014). The density of the gas-particle
173 mixture, hence particle volumetric concentration and mass flow rate, do not change with respect to
174 the conduit exit.
175 The experiments were monitored with a network of multiple high definition videocameras (recording
176 at 50 frames per second) and pressure sensors, which allowed measurements of the jet speed and
177 geometry (including heights, lengths and volume) and speed and dynamic pressure of the density
178 currents formed after the jet impact on the ground.
179 A frame of the close-up view of the passage of an experimental current is shown on Fig. 5, with insets
180 of average flow velocity, shear velocity, and dynamic pressure values. In the figure, the current
181 thickness is also shown and the position of a pressure sensor is indicated.

182 The shear velocity of the density currents was calculated following the method of Dellino et al., 2008,
183 by means of the law of the wall of a turbulent shear flow moving on a rough substrate: $u_{avg}(y) = u_*$
184 $\left(2.5\ln\frac{H_T}{k_s} + 6.5\right)$ (9)

185 where k_s= 1 cm is the substrate roughness as measured on the ground, H_T is current thickness and
186 $u_{avg}(y)$ is the height-averaged current velocity measured at flow front by video analysis.
187 The mass flow rate at the impact of the jet on the ground was calculated by means of Equation (1),
188 by assuming that it was conserved along the ascending descending jet trajectory (Dellino et al., 2014).
189 The particle volumetric concentration of the current was calculated by equation (2), by means of the
190 known gas and particle densities. The current density ρ_{mix} was calculated by dividing the mass flow
191 rate by the average velocity. The mass flow rate in the current was calculated, at each location, by
192 subtracting the mass of sediment deposited at previous locations from the mass flow rate at the impact,
193 and using as the cross-sectional area of the flow, the value measured at each location by multiplying
194 H_T for $2\pi L$, where L is the distance, from the impact, reached by the flow front.
195 The particle volumetric concentration in the jet, C_1 ranged between 0.019 and 0.063, as it was
196 measured by the ratio of total particle load and jet volume (see Tab. 1). At the passage from the
197 sedimentation of the descending jet to the sedimentation of the density current, the particle volumetric
198 concentration in the gas-particle mixture, C_2 decreases (see Tab. 1). It decreases also along the current
199 runout as a consequence both of sedimentation and of increase of the cross-sectional area of the flow
200 at increasing distance.
201

202 **3. Results**

203 ***3.1 Generation, evolution and deposition of experimentally-generated PDCs***

204 The collapsing gas-particle jet, on hitting the ground (Fig. 4b), resembles the collapse of a natural
205 eruption column leading to the formation of pyroclastic density currents. Upon impact, the jet is more
206 than one meter wide and leaves on the ground a tens of centimetre thick deposit (Fig. 4c). The collapse

occurs on the right side because of the slight inclination of the conduit. This condition allowed the formation of a column impacting on the ground and not falling back in to the conduit. The thickness of the deposit decreases from the centre of the impact to the margin, with a shape approximating a cone. At the centre of the impact the deposit is massive, and does not show any visible sedimentary structure related to shear movement (Fig. 4d). The deposit at the margin of the impact, while decreasing in thickness, starts to show some undulations (Fig. 4c), similar to ripples, likely to be attributed to an incipient shear movement. In the case of fine-grained experimental runs, no tractive structures are formed, neither at the impact (Fig. 4e), nor at distal locations (Fig. 4f). Similar characteristics are reported in natural fine-ash deposits, which show a monotonous, structureless facies, with no grain-size variation along runout (e.g., Branney and Kokelaar, 1997; Dartevelle et al., 2002; Kokelaar et al., 2007).

After the impact of the fountain on the ground, the normal stress of the fluid is transformed into a tangential stress, leading to a shear flow that evolves laterally into a few meters thick, fully turbulent, gas-particle current, moving at several m/s (Fig. 6a). It spreads for more than 20 m over the zone of the impact and leaves on the ground a thin bed (a few cm thick) formed by the sustained alimentation of the sediment flux from the collapse. When the run is fed with the pyroclastic material of the coarser composition, the thin layer shows ripple-like sedimentary structures (Fig. 6b), which demonstrate that the bedload was moved at a rate sufficient to form tractional bedforms. The structures represent the lateral evolution of the undulations visible at the lateral margin of the impact.

A close-up view of two frames at the current front (Fig. 6c and d) shows the progressive shearing effect that the tangential stress exerts on the particles of the bedload, which favours the formation of ripples.

The ripple structures are characterized by an asymmetrical distribution of particles: the finer sizes occur at the foreset and the coarser ones at the backset, implying that the transportation process, in the shear current, is selective in terms of grain size. This suggests that the finer particles rested in

232 the shadow zone within the ripple troughs. These features are similar to those shown by natural
233 pyroclastic density currents (Sulpizio et al., 2014).
234 Some variants of the ripple structures were observed in the experimental deposits. Centimetre-thick
235 structures that show an average wavelength about 30cm (Fig. 6b) are found in locations a few metres
236 outside the impact zone. They are associated to fast currents (u_{avg} =13 m/s; u_*=0.73 m/s, 0.0035 C in
237 the example of Fig. 6b) and are made up of coarse ash and lapilli (median size D_{sm} = 0.79 mm in the
238 example of Fig 7b). Other cm-thick narrowly spaced ripple-like structures, showing an average
239 wavelength of about 8 cm, are also found a few metres outside the impact zone. The ripples are made
240 of coarse ash and lapilli, (median size D_{sm} = 1.69 mm in the example of Fig. 6e) and are associated
241 to a lower current speed (u_{avg} = 6.3 m/s, u_*=0.38 m/s in the example of Fig. 6e). An average
242 wavelength of 20 cm is shown by mm-thick ripples found in distal locations, more than 10 m outside
243 the impact zone. They are made of medium ash (median size D_{sm} = 0.26 mm in the example of Fig.
244 6f), and are formed by slow currents (u_{avg} =3.9 m/s, u_*=0.19 m/s, in the example of Fig. 6f). Such
245 data suggest that the spacing and thickness of tractional features are somehow linked to the flow
246 regime and grain size of the particulate material, as it is postulated for sedimentary currents (Lowe,
247 1988; Postma et al., 2009; Cartigny et al., 2014). It is, however, quite difficult to find a consistent
248 relationship between speed, spacing and grain size in the distal deposits, especially in the case of gas-
249 particle currents (Middleton, 1984).
250 In further locations that were reached by the flow at the time the fountain had stopped feeding the
251 current (Fig. 7a), only fine-ash material, lacking sedimentary structures, was deposited. This material
252 is spread well over the blue plastic sheets and formed a submillimetric veil of ash (Fig. 7b) that
253 represents the waning-flow washload.
254 A general facies model of the experimental deposits, associated to the flow evolution along runout,
255 is shown on Fig. 8. The proximal facies is massive and lays at the center of the impact. The proximal-
256 transitional facies shows some incipient shear structures at the surface and is formed around the lateral
257 zone of impact, where the flow rate developed basal shear stress. The medial facies is associated to

the fully turbulent, fast, shear current and is characterized by coarse-ash ripple-like bedforms. The distal facies is associated to the down-current evolution of the flow, where velocity decreases and the particle load is less concentrated and finer grained, resulting in ripple-like structures of medium ash. The ultra-distal zone is associated to the waning stage of the flow where the wash load is slowly settled and forms a thin, structureless, fine-ash bed.

3.2 Scaling between experimental and natural currents

The obvious difference between the experiments and natural pyroclastic density currents is the much larger thickness of natural layers, which results from the vertical aggradation of multiple laminae, formed during the time-integrated passage of thick (up to hundreds of meters), expanded currents, which in nature last much longer (several minutes up to hours) than the experiments, the latter lasting up to 30 s. In the natural case, the passage of a long-lasting pyroclastic density current is likely to generate a vertical facies association (Mele et al., 2015), also depending on the evolution of the eruption feeding the collapsing column, which is not considered here.

Notwithstanding these differences, the values of the fluid-flow parameters of the experiments are in the same order of magnitude of natural pyroclastic density currents, suggesting that a scaling between experiments and nature can be proposed. For example: i) the specific mass flow rate at conduit exit was up to 4000 kg/m^{2}s; ii) the current velocity was up to 13 m/s; iii) the Reynolds number $Re_* = \frac{\rho_f u H_T}{\mu}$, with μ fluid viscosity, was always in excess of 10^6, meaning the flow was fully turbulent. Furthermore, shear velocity (up to 0.73 m/s) and dynamic pressure (up to about 500 Pa) are almost comparable to those calculated for some natural pyroclastic density currents (Mele et al., 2011 and 2015). The experimental deposits share some features with the natural counterparts, for example: i) the deposit at the centre of the impact looks similar to the layer deposited by massive pyroclastic flows (Bursik and Woods, 1996; Branney and Kokelaar, 2002); ii) dilute pyroclastic density current deposits have bedforms that are visually similar to those found in the experiments (Sulpizio et al., 2014); iii) the facies model of the experimental deposits of Fig. 8 is similar to what is observed in

284 some ignimbrites (e.g., Vazquez and Ort, 2006; Brown and Branney, 2013; Wright et al., 2016); iv)
285 the contemporaneous occurrence of massive and stratified deposits related to both concentrated and
286 dilute currents has been already noted in volcanology (Druitt et al., 2002; Gernon et al., 2013; Breard
287 et al., 2016; Breard and Lube, 2017).
288
289 **4. Modelling of the sedimentation and bedload transportation rates**
290 In order to identify the threshold ratio that marks the transition between massive and stratified
291 deposits, the sedimentation and bedload transportation rates were calculated at multiple locations
292 along runout. They include the impact point, as for recording the formation of the thick massive
293 layer, and further locations, where the turbulent suspension current lead to the sedimentation of the
294 stratified beds. A total of 13 locations are considered in this paper, 5 out of them represent as many
295 thick massive layers formed at the impact, and 8 represent beds formed by the turbulent suspension
296 currents. The experimental deposits were sampled as for obtaining the particle parameters to be
297 used in the calculation of S_r and Q_b. They include grain size, density and componentry.
298
299 ***4.1 Methods and measurements used in the calculation of S_{rw} and Q_b***
300 The sedimentation rate S_r (see Tab. 1) was measured as the mass sedimented per unit area (the latter
301 being obtained by an area-integrated sample of sediment), over the time of sedimentation, which was
302 measured by using the time length of the video-frames between the arrival of the current and the end
303 of the jet feeding the current.
304 For the thick, massive deposits, the sedimentation rate S_r ranged between 39 and 220 $kgm^{-2}s^{-1}$; while
305 it ranged from 0.19 to 1.17 $kgm^{2}s^{-1}$ for the deposits with ripple-like tractional structures. It was about
306 0.022 $kgm^{-2}s^{-1}$ for the thin structureless fine-ash beds.
307 The bedload transportation rate was calculated by modifying the model of Wilcock and Crowe 2003,
308 which is based on flume experiments. In the model, a correlation between W_i^* (Equation 5) and the
309 shear stress τ at the base of the current is introduced

310 $$W_i^* = \begin{cases} 0.002\xi^{7.5} \, for \, \xi < 1.35 \\ 14\left(1 - \frac{0.894}{\xi^{0.5}}\right) for \, \xi \geq 1.35 \end{cases} (10)$$

311 with

312 $$\xi = {}^{\tau}/_{\tau_{ri}} (11)$$

313 where the shear stress at the base of the current τ, was calculated by the relation $\tau = \rho_{mix} u*$.

314 τ_{ri} is the minimum shear stress needed to move by traction the i_{th} size fraction; ${}^{\tau_{ri}}/_{\tau_{rsm}} = ({}^{D_i}/_{D_{sm}})^b$,

315 where τ_{rsm} is the minimum shear stress needed to move the bedload mixture by traction, with $b =$

316 ${}^{0.67}/_{1 + \exp(1.5 - {}^{D_i}/_{D_{sm}})}$, D_i the diameter of the i_{th} size fraction and D_{sm} the diameter of the

317 median size of the grain-size distribution of the bedload material; $\tau^*_{rsm} =$

318 ${}^{\tau_{rsm}}/_{({}^{\rho_S}/_{\rho_f} - 1) g \rho_f D_{sm}}$ with τ^*_{rsm} the critical Shields number normalized to the mixture of the

319 bedload material. $\tau^*_{rsm} = 0.75\theta_{tmedian}$ where $\theta_{tmedian}$ is the critical Shields number of the median

320 size. The critical Shields number $\theta_t = \frac{\rho_f u_*^2}{Dg(\rho_s - \rho_f)}$ is the ratio of surface to volume forces and represents

321 the threshold of initiation of motion of particles resting on the substrate. It is a function of the

322 Reynolds' number of shear $Re_* = \frac{\rho_f u_* D_{sm}}{\mu}$. The critical values, for various fluids, including liquids

323 and gas, are found in the review of Miller et al. (1977).

324 In the original Wilcock and Crowe 2003 model the relation $\tau^*_{rsm} = 0.021 + 0.015\exp[-20F_s]$

325 was used, with F_s representing the percent of sand in the sediment. In this paper, as resulting from

326 our tests on volcanic material, a value of 0.75 of the critical Shields number of the median size

327 $\theta_{tmedian}$ was used, as representing the critical Shields number normalized to the mixture of the

328 bedload material τ^*_{rsm}. The value of the Shields number of the median size was derived from the

329 Miller et al., (1977) curve for gas. It ranged from 0.010 for the fastest, coarse grained, currents to

330 0.019 for the slowest fine-grained current that formed thin structureless fine-ash beds.

331 The procedure for the calculation of *Qb* starts with the analysis of the multicomponent grain-size
332 distribution of the deposit. For each size fraction and component (glass, lithics and crystals) the
333 critical shear stress for the initiation of motion is calculated and the ratio between the shear stress at
334 the base of the current and the critical shear stress is calculated for each size class. Equations (10)
335 and (5) are used to calculate the bedload transportation rate of each size class, q_{bi}. The total bedload
336 tansportation rate per unit width Q_b is obtained by summation of the bedload transportation rate of all
337 size classes.
338 With the aim of illustrating step by step the calculation of Q_b, in the supporting files A, B and C,
339 examples of calculation of a massive layer at the impact; a layer showing ripple-like tractional
340 structures and a thin structureless fine-ash bed are reported, respectively. Grain size, density and
341 componentry data are included.
342 The bedload transportation rate data are reported in Tab. 1. It ranged from 9.3×10^{-5} m^2s^{-1} to 2×10^{-3}
343 m^2s^{-1} for the massive layers, while it ranged from 7.4×10^{-6} m^2s^{-1} to 1.15×10^{-3} m^2s^{-1} for the layers
344 with ripple-like tractional structures. It is 1.77×10^{-7} m^2s^{-1} for the thin structureless fine-ash beds.
345
346 ***4.2 The threshold ratio of sedimentation and bedload transportation rates and the discriminatory***
347 ***diagram between massive and stratified deposits***
348 In order to compare sedimentation and bedload transportation rates easily, they need to be
349 expressed in the same physical dimension (m^2s^{-1}). For this purpose S_r has been transformed into the
350 volumetric sedimentation rate per unit width, S_{rw} by the formula of transformation
351 $S_{rw}=A_r Ref_a Ref_w$ (12)
352 The transformation of Equation (12) starts by first calculating the growth rate of sediment thickness
353 A_r (ms^{-1}) by means of equation (7). A square of one meter width is considered as the reference area
354 on the ground, Ref_a, which is the same area on which Q_b is calculated. By means of the
355 multiplication of A_r for the reference area (which is one square meter), the volumetric sedimentation

356 rate is obtained (m^3s^{-1}). By dividing the volumetric sedimentation rate by the width of the reference
357 area, Ref_w (which is one metre), we obtain S_{rw} (m^2s^{-1}), which has the same dimension of Q_b.
358 Upon calculation of S_{rw} and Q_b, we verified that: i) the ratio of particle volumetric concentration C_1
359 in the impacting fountain that fed the massive layer, and ii) the particle volumetric concentration
360 transported in the suspension current C_2 at the first location after the impact are a function of the
361 ratio of Qb^*/S_r, which is defined by:

362 $$\frac{C_1}{C_2} = 0.5581\left(\frac{Q_b^*}{S_r}\right)^{-0.578} \quad (13)$$

363 where $Q_b^* = Q_b\frac{D_{sm}}{1mm}$ is the bedload transportation rate normalised to a grain size of one millimetre.
364 Data of C_1, C_2, Q_b^*, Q_b, D_{sm}, S_{rw} and S_r are found in Tab. 1. The trend of equation (13) is illustrated
365 by Fig. 9. Equation (13), being based on a single data set, would need further investigation for proving
366 its general validity. It can be useful for back calculating the concentration in the dense eruption
367 column, starting from the concentration in the current, once the sedimentation and bedload
368 transportation rates are known, which could help in the reconstruction of the *MER* of past eruptions.
369 Data of the sedimentation rate per unit width of the experiments are listed in Tab. 1. They range
370 from 0.030 m^2s^{-1} to 0.2 m^2s^{-1} for the massive layers and from $8.2x10^{-5}$ m^2s^{-1} to 9.75^{-3} m^2s^{-1} for the
371 layers with ripple-like tractional structures. It is $1.78x10^{-5}$ m^2s^{-1} for the thin structureless fine-ash
372 beds.
373 Experiments suggest that massive and stratified layers form under different conditions of bedload
374 transport and sedimentation, and that the abundance of very fine material, and particle volumetric
375 concentration, have an influence in the formation of deposit structures. This is similar to what has
376 been already suggested by Lowe (1988) for subaqueous density flows. Our results indicate that in the
377 thick massive beds formed at impact, where no shear structures are visible, S_{rw} is at least 100 times
378 larger than Q_b (see Tab. 1). These data suggest that the threshold limit between the conditions leading
379 to the formation of massive vs stratified deposits can be represented, in a Q_b vs S_{rw} diagram, as the
380 line of S_{rw}=100Q_b. Such a diagram is shown on Fig. 10, with the massive beds formed at impact

plotting below the threshold limit on the right-hand side, where both the sedimentation rate per unit width and the bedload transportation rates are high. Also the thin structureless fine-ash beds formed by dilute currents plot below the threshold limit, on the left-hand side of the diagram, where both the sedimentation rate and bedload transportation rates are very low. This means that both with high and low sediment flux a value of S_{rw} lower that 100 Q_b inhibits the formation of tractional features in the deposit. In the thin structureless fine-ash beds, the absence of tractional features indicates that, although the sedimentation rate is very low (see Tab. 1), the shear stress was not effective in moving the bedload material. This is due to the very high value that the critical Shields number θ_t reaches where the shear Reynolds number is lower than 1 for gas, as it is shown in the diagram of Miller et al., (1977). In the case of the structureless fine-ash beds of the experiments, the shear Reynolds number is about 0.9 and the critical Shield number is 0.19, much higher than that of the coarse-ash ripple layers, which is 0.10. This means that very fine volcanic ash, as for other fine sedimentary materials, is difficult to be moved by traction because it is cohesive and exposes a limited surface to the shear stress (Zanke, 2001; Manning and Schoellhamer, 2013; Xu et al., 2015). This outcome can help interpreting the origin of structureless finely-grained pyroclastic deposits. In fact, structureless fine-ash beds are not necessarily and univocally the result of fallout processes from a convective eruptive column (as it is frequently assumed in volcanology), but likely the far facies left from pyroclastic density currents, also known as co-ignimbrite ash plumes (Bursik and Woods, 1996). It has implications in the assessment of the eruptive history and, hence, hazard of active volcanoes.

S_{rw} of the layers with ripple-like structures is much lower than that of the massive deposits (and of the fine-ash structureless beds). For these layers, the ratio S_{rw}/Q_b is always lower than 100, and deposits plot above the line of $S_{rw}=100Q_b$ of Fig. 10. In the diagram of Fig. 10, deposits with ripple-like structures of different wavelength and height are also discriminated, and a line separating the field of widely spaced vs narrowly spaced ripples is tentatively set at $S_{rw}=4Q_b$. This suggests that, while it is difficult to rationalize the dependence of bedform scale in terms of grain size and speed (as noted in the introduction section), it seems that the wavelength and height of sedimentary

structures can be better followed by the ratio between sedimentation and bedload transportation rates.

Even though the numerical limits of Fig. 10 would need additional tests to verify their precision and general validity, the rationale on which the diagram is based is to be noted, i.e.: "that is the balance between sedimentation and transportation rates that controls deposit structures". This outcome, which is confirmed by experiments, encourage application to natural cases.

5. Application to natural deposits

Campi Flegrei and Vesuvius in Southern Italy (Fig. 11) represent the most hazardous explosive volcanoes in Europe. The deposits investigated in this paper come from the 4.2 ka Plinian eruption of Agnano Monte-Spina at Campi Flegrei (de Vita et al., 1999; Mele et al., 2015) and from the 8.2 ka Plinian eruption of Mercato at Vesuvius (Mele et al., 2011). The sedimentation and bedload transportation rates were calculated as to both test the applicability of the discriminatory diagram of Fig. 10 to natural deposits, and to verify its utility in the reconstruction of the physical parameters of the eruptions.

The sedimentation rate of deposits was reconstructed by means of the model of Dellino et al., (2019)

$$S_r = \left(\sum_i^n \rho_{s_i} w_{t_i} \left(\frac{\frac{\phi_i / \rho_{s_i}}{\sum_{i=1}^{n} \phi_i / \rho_{s_i}} * C_{tot}}{\left(\left(10.065 * \frac{P_{ni}}{P_n^*} \right) + 0.1579 \right)} * 0{,}7 + \frac{\frac{\phi_{i+1} / \rho_{s_{i+1}}}{\sum_{i=1}^{n} \phi_{i+1} / \rho_{s_{i+1}}} * C_{tot}}{\left(\left(10.065 * \frac{P_{ni}}{P_n^*} \right) + 0.1579 \right)} * 0.3 \right) \right) - 0{,}01 \quad (14)$$

that was developed starting from experiments of which the ones used in this paper represent a subset. $P_{ni} = w_{ti}/ku_*$ is the Rouse number of the i_{th} size fraction of the solid material suspended in the current with k the Von Karman constant (0.4). The Rouse number defines the particle volumetric concentration as a function of flow height, by means of

$$C_{tot} = C_0 \frac{1}{H_T - y_0} \int_{y_0}^{H_T} \left(\frac{H_T - y_0}{y_0} \frac{y}{H_T - y} \right)^{P_{nsusp}} dy \quad (15)$$

where C_{tot} is the total concentration of the current averaged over total flow thickness H_T. C_0 is a value of known concentration at a specific height y_0, which is generally assumed very close to the ground (Middleton, 1984). P_{nsusp} is the Rouse number associated to the maximum concentration that can be held in suspension. $P_n{}^*$ is the normalized Rouse number, which is obtained by the ratio of $P_{n_{avg}}/P_{nsusp}$, with $P_{n_{avg}} = \sum_{i=1}^{n} P_{ni} C_i / C_{tot}$ being the average Rouse number of the particulate material.

The bedload transportation rate of deposits was calculated by means of Equations (5) and (10).

The flow input parameters used for the calculation of the sedimentation and of the bedload transportation rates of the Mercato and Agnano Monte-Spina density currents (i.e. shear velocity, shear stress and particle volumetric concentration), were derived from Mele et al., (2011) and Mele et al. (2015), respectively. These input parameters (see Tab. 2) were calculated by means of the PYFLOW code (Dioguardi et al. 2014, 2018). PYFLOW solves for the flow properties of turbulent pyroclastic density currents based on the approach first presented by Dellino et al. (2008). The calculation utilizes the concept of hydraulic equivalence, which states that if two components (for example vesicular glass and crystals) that have different median size, density and shape, coexist in a deposit, it means they were settling from suspension with the same settling velocity (Jutzeler et al., 2015). By the assumption that sedimentation occurs when the settling velocity approaches current shear velocity (Middleton, 1984), the software equates the settling velocity of the two components and solves for the current shear velocity u_*, total concentration C_{tot} and Rouse number at maximum suspension capacity Pn_{susp}, with y_0 obtained numerically (Dellino et al., 2008). Input parameters of particles: multicomponent grain-size distribution, density and drag coefficient, are obtained by laboratory investigations on sediment samples. The settling velocity, w_t was calculated by means of the model of Dioguardi et al. (2018). PYFLOW gives on output the probability density functions of each flow parameter. In the present study, the values of the average solution were utilized (see Tab.2).

4.1 The B2 Agnano Monte-Spina pyroclastic density current

The deposits of Agnano Monte-Spina refer to the pyroclastic density current of the eruption phase B2. This phase followed the fallout layer of the Plinian convective column of phase B1 (de Vita et al., 1999; Mele et al., 2015). B2 phase resulted from a dense eruptive column that on impact, which occurred on an almost flat surface, generated a massive deposit. As the result of the lateral evolution of the impact, a thick, dilute pyroclastic density current was formed, which generated stratified deposits with dune-like bedforms. The fine-ash component, which represents a substantial hazard at Campi Flegrei, spread well away the caldera border. The most proximal outcrops of B2 are found at Vallone del Corvo and at Sbirri (Fig. 12a and b), two localities beneath the Agnano Monte-Spina caldera rim. At Vallone del Corvo a 8 m thick, poorly sorted, massive deposit, composed of lapilli and scattered scoriaceous bombs supported in an ash matrix crops out (Fig. 12b). Alignments of coarse clasts occur at various levels, suggesting some incipient basal shear. At Sbirri, a 4 m thick (Fig. 12c), poorly sorted, massive bed composed of lapilli and scattered bombs, supported in an ash matrix, occurs, and is correlated with the deposit at Vallone del Corvo. The deposit is overlain, conformally, by a 1.5 m thick stratified deposit of ash and lapilli showing some normal grading, likely due to variations, over time, in the feeding of the eruption column. The stratified deposit has a low angle internal bedding, which is typical of volcanic bedforms (Crowe and Fisher, 1973), and shows small-dune bedforms (in the sense of Ashley, 1990) with wavelength about 2 m and 0.15 m height (Fig. 12c). The massive bed at Vallone del Corvo can be interpreted as formed by the impact of the dense gas-particle column that fed the eruption. In contrast, the massive layer at Sbirri can be interpreted as resulting from the lateral zone of the fountain impact, where the incipient lateral movement on the ground generated, afterward, the turbulent shear current that lead to stratification.

Moving away from the caldera rim, the next locality where a stratified deposit with bedding structures of the same unit B2 occurs, is at Verdolino (Fig. 12d), about 2 km from the caldera rim. The deposit is much finer and thinner compared to the stratified one at Sbirri. The layer is composed of coarse and fine ash, has a low-angle internal bedding, and includes ripple structures of coarse ash with wavelength about 0.5 m and height about 0.05 m. The deposit can be interpreted as formed from the

480 down-flow evolution of the dilute suspension current. The most distal outcrop of B2 is at Camaldoli
481 (Fig. 11e), which is about 4 km from the caldera rim and shows a 0.2 m thick structureless fine-ash
482 bed.
483 The facies architecture of B2 is quite similar with that defined by the analogue experiments on figure
484 8. The deposit at Vallone del Corvo looks similar to the proximal facies of the impact zone; the
485 deposit at Sbirri represents the proximal-transitional facies; the stratified deposit at Verdolino is
486 similar to the distal facies and the fine-ash structureless bed at Camaldoli represents the ultra-distal
487 facies of the washload settling from the waning current.
488
489 ***5.1.1 Use of the discriminatory diagram with the proximal and transitional facies of deposits and***
490 ***reconstruction of the mass eruption rate of B2***
491 Judging from the vicinity of the two outcrops to the caldera rim, it is reasonable to hypothesize that
492 the sedimentation of the massive layer at Vallone del Corvo and at Sbirri resulted from the direct
493 feeding of the mass flow rate of the collapsing column. The bedload transportation rate Q_b of the
494 massive layer was calculated by means of Equations (5) and (10). As input parameters, the shear
495 velocity u_{*1}, flow density ρ_{mix1}, shear stress τ and grain-size distribution of the deposit were needed.
496 As for the flow density of the gas-particle mixture forming the massive layer, which is $\rho_{mix1} = \rho_s C_1$
497 $+ \rho_g(1 - C_1)$, it is reasonable to assume that it must have been higher than that of the lateral dilute
498 current $\rho_{mix2} = \rho_s C_2 + \rho_g(1 - C_2)$, which formed the stratified layer with small-dune bedforms. The
499 difference between ρ_{mix1} and ρ_{mix2} is due to the lower particle volumetric concentration of C_2 with
500 respect to C_1. The latter was calculated by using as C_2, in equation (13), the value obtained for the
501 dilute current at Sbirri by Mele et al. (2015), which is 0.001 (see Tab. 2) and using 0.01 as the value
502 of $\frac{Q_b}{S_{rw}}$, which is the minimum value for the formation of a massive layer. The resulting value of C_1 is
503 0.009.

Since both the massive and the stratified deposits at Sbirri result from the incipient impact of a dense eruptive column, the shear stress acting on the massive layer $\tau = \rho_{mix1} u_{*1}^2$, and that leading to the formation of the lateral dilute current $\tau = \rho_{mix2} u_{*2}^2$, have to be similar. By means of the values of τ, ρ_{mix2} and u_{*2}^2 that were calculated by Mele et al. (2015) for the lateral dilute current that formed the stratified layer at Sbirri (see Tab. 2), and using the value of C_1 previoulsy obtained, the value of u_{*1} was calculated. With these input values, and by the use of the grain-size distribution of the massive layer, a value of 0.015 m^2s^{-1} was obtained for Q_b. See the supporting file D for a step by step calculation. By setting the value of $S_{rw}=100Q_b$, the value of S_{rw} was calculated as 1.5 m^2s^{-1}. With these values, the thick massive layer at Sbirri plots, in the discriminatory diagram of Fig. 10, in the same position of the thick massive layers from experiments.

For the stratified layer with small-dune bedforms at Sbirri, by using as input parameters in Equation (14) those calculated by Mele et al. (2015) (see Tab. 2), a sedimentation rate S_r of 0.59 $kgm^{-2}s^{-1}$ resulted. The step by step calculation of S_r is found in the supporting file E. By means of Equation (12), S_r was converted into S_{rw}, with a value of 0.00047 m^2s^{-1} (see Tab.1). As for Q_b of the small-dune bedform layer at Sbirri, it was calculated by means of Equations (5) and (10) and using as input parameters those calculated by Mele et al. (2011), see Tab. 2. The resulting value of Q_b was 0.022 m^2s^{-1}. With the calculated values of Q_b and S_{rw}, the layer with small-dune bedforms at Sbirri plots in the discriminatory diagram of Fig. 10 in the field of stratified deposits, with a lower S_{rw}/Q_b ratio compared to the experimental deposits. The structures of the stratified layer at Sbirri have a much longer wavelength, about 2 m, and height, about 0.15 m, (see Fig. 12c) with respect to the ripple-like structures of experimental deposits. The position of the small-dune bedforms at Sbirri confirms the inverse relationship between bedform scale and S_{rw}/Q_b ratio, and extends the range of the diagram of Fig. 10 to lower S_{rw}/Q_b values and larger bedforms.

With the data obtained on the massive and stratified deposits at Sbirri, an evaluation of the *MER* of the B2 phase of Agnano Monte Spina can be obtained. An estimation of *MER* can be obtained by the total volume of deposits divided by the duration *t* of deposit aggradation. An approximate volume of

0.15 km^3 has been proposed for the B2 deposit by Dell'Erba (2004). As for t (the time of deposit aggradation), it is reasonable to hypothesize that the stratified layer at Sbirri represents deposition from the continuous aggradation of the lateral current that was fed from the eruption column. The time of deposit aggradation was calculated as $t= d/ S_r/\rho_{dep}$, where d=1.5 m, is the thickness of the stratified layer and ρ_{dep} is 1248 kgm^{-3}, as measured in the laboratory after extracting a known volume of deposit in the field and weighing it. S_r, as obtained previously, was set to 0.59 $kgm^{-2}s^{-1}$. The resulting *MER* is about $6x10^7$ kg/s. In this estimation, the assumption is made that neither contemporaneous ash fallout nor additional layers (unrecorded in the field) where formed during B2 phase. The value is therefore to be considered as a minimal *MER*.

To constrain this figure of the *MER* of B2, a complementary method was applied. It is based on the assumption that the massive layer at Sbirri is the result of the direct sedimentation from the lateral zone of the impact, which was followed, in stratigraphic continuity, by the formation of the stratified layer. Following the hypothesis that the eruption column collapsed completely and, as introducted earlier, in its ascending-descending trajectory it did not entrain air and followed Bernoulli's equation, V_0, ρ_{mix} and C_0 at the vent are respectively equal to the velocity U_f, density ρ_{mix} and particle volumetric concentration C_1 of the eruption column at the impact on the ground.

$$MER/\pi r^2 = V_0 \rho_s C_1 \quad (16)$$

is the *MER* per unit area at the vent, with πr^2 the vent cross-sectional area. When air entrainment is neglected in the eruption column, density doesn't change along the ascending descending trajectory, and the mass flow rate per unit area at the vent is equivalent to the area specific mass flow rate Q_s of the gas-particle mixture feeding the massive layer at the impact

$$Q_s=\rho_s C_1 U_f \quad (17).$$

From the equality of (16) and (17)

$$MER = \rho_s C_1 U_f \pi r_0^2 \quad (18).$$

554 By assuming that particles fall at the same descent velocity of the collapsing column (meaning a
555 mechanical coupling between particles and fluid in the dense fountain), it results that $U_f = A_r/C_1$
556 where A_r is the aggradation rate of the massive deposit. By means of Equation (12), the aggradation
557 rate A_r is obtained by the previously calculated value of S_{rw} of the massive layer. A_r is about 1.53 m/s
558 and the falling velocity of the fountain $U_f = A_r/C_1$is about 170 m/s. As for C_1, the value of 0.009
559 previously calculated for the massive layer was used. From the equality of Equations (16) and (17),
560 U_f represents also the exit velocity V_0 of the gas-particle mixture at the vent.
561 Finally, using, in equation (3), the values of ρ_{f1} and V_0, and setting the value of Fr'_0 between 1 and
562 3, which is the range proposed by Dellino et al. (2014) for completely collapsing eruption columns,
563 a range of *MER* was obtained, which is shown on Fig. 13 as a function of the Froude number. The
564 *MER* value of $6x10^7$ kgs^{-1} previously obtained (by dividing the total mass of deposit by the time of
565 layer aggradation), falls inside the range of Fig. 13 and corresponds with a vent radius of 85 m. Both
566 the radius, the *MER* and the exit velocity are compatible with the values generally considered in the
567 literature (Dellino et al., 2010 and 2014). It is to note that the specific mass flow rate at the vent is in
568 the order of $3x10^3$ $kgm^{-2}s^{-1}$, which is in the range of values obtained in experiments, further justifying
569 the scaling between natural and experimental cases.
570
571 ***5.1.2 Use of the discriminatory diagram with the distal and ultra-distal facies of deposits for the***
572 ***reconstruction of fine-ash deposition of B2***
573 The distal facies of B2 cropping out at Verdolino has a Q_b value of 0.0029 $m^{-2}s^{-1}$ and S_{rw} of 0.00015
574 $m^{-2}s^{-1}$ (see Tab. 1). They were calculated, respectively, by means of Equations (10) and (5) and of
575 Equation (14). Data from Mele et al. (2011) were used as input (see Tab. 2). The deposit shows
576 coarse-ash ripple structures with a wavelength about 0.5 m and height about 0.05 m (Fig. 12d), which
577 are a little larger than the ripple beds of the experiments. The Verdolino deposit, by plotting, in the
578 diagram of Fig. 10, in a position characterized by a slightly lower value of S_{rw}/Q_b when compared to

579 the ripple beds formed by experiments, confirms the inverse relationship between S_{rw}/Q_b and bedform
580 scale.
581 As for the current that formed the fine-ash structureless deposit of the ultra-distal facies of B2
582 cropping out at Camaldoli, it is expected that a pyroclastic density current, due to the continuous air
583 entrainment along runout, expands during its down-flow evolution. It can be hypothesized, therefore,
584 that the thickness of the current, at Camaldoli, could not have been lower than that calculated by Mele
585 et al. (2015) at Verdolino (see Tab. 2), which is about 300m. This value can be used as the minimum
586 height H of the current at Camaldoli. Following the approach of Lajoie et al. (1989) and Dellino et
587 al. (2008), who suggest that in steady conditions $C= d/H$, a particle volumetric concentration of C=
588 0.0006 results at Camaldoli, which can be considered as a maximum. P_{nsusp} was calculated
589 numerically as 0.83 by using the values of d, C and H as y_0, C_{tot} and H_T in equation (15). By the use
590 of P_{nsusp}, ρ_{mix} and the grain-size distribution at Camaldoli, and setting the condition $S_{rw}=100Q_b$ as
591 the minimum value for obtaining a structureless fine-ash bed (since the deposit does not show any
592 shear structure), the combined use of Equations (10) and (14) resulted in values of u_*, τ, S_{wr} and Q_b
593 at Camaldoli about 0.43 ms^{-1}, 0.34 Pa, $6.7x10^{-5}$ m^2s^{-1} and $6.7x10^{-7}m^2s^{-1}$, respectively (see Tab. 1).
594 With the values of Q_b and S_{rw}, the fine-ash structureless bed of Camaldoli plots in the low-left corner
595 of diagram of Fig. 10, in a similar position of the fine-ash structureless beds of the experiments.
596 When S_{rw} is transformed into S_r by means of Equations (7) and (12), a value of the sedimentation rate
597 of $9.6x10^{-2}$ $kgm^{-2}s^{-1}$ results. The aggradation rate A_r is $6.7x10^{-5}$ ms^{-1}, and the deposition time t is about
598 3000 s. Step by step calculation can be found in the supporting file F. Such a value of deposition time
599 must be considered as a minimum since, by hypothesizing a thicker current, the concentration would
600 be lower, the sedimentation rate would further decrease, and the deposition time would increase.
601 This means that in ultra-distal localities, as at Camaldoli, the area is engulfed, for almost an hour,
602 with a fine-ash cloud moving slowly on the ground. While the cloud loses much of its mechanical
603 and thermal destructive power along runout, it is still rich of very harmful to breath fine material,
604 which could compromise human survival also in zones well outside the Campi Flegrei caldera.

605

606 *5.2 Rheology and mobility of Mercato massive undercurrent*

607 The stratigraphy of Mercato eruption at Vesuvius (Mele et al., 2011), is made up of alternating Plinian
608 fallout layers and pyroclastic density current deposits that are well exposed in the northern sector of
609 the volcano, at the rim and down the slope of Monte-Somma (Fig. 14a). The deposits considered in
610 this paper are from the first phase of the eruption and consist of a m-thick poorly-sorted massive layer
611 of lapilli and scattered bombs and blocks supported in an ashy matrix (Fig. 14b), and a distal deposit
612 made of a stratified lapilli deposit exhibiting small-dune bedforms (Fig. 14c). Both result from a
613 dense eruption column that impacted, upon collapse, on the uneven slope of the volcanic cone. The
614 massive layer is interpreted as fed and formed directly from the sedimentation of the collapsing
615 column, whereas the stratified layer is interpreted as formed by the dilute current derived from lateral
616 evolution of the flow after impaction on the ground. Along the gullies departing from the volcano,
617 the thick massive deposit, aided by the steeper slope, moved as a highly concentrated debris flow,
618 independent from the faster, more dilute, overcurrent. The contemporaneous occurrence of a massive
619 underflow together with a dilute overcurrent has already been reported at other localities (Druitt et
620 al., 2002; Gernon et al., 2013; Breard and Lube, 2017).
621 The massive facies terminates at the base of the cone where, as a response of the drastic decrease of
622 the slope angle, it "freezes" abruptly in a 2 m thick layer (Fig.14 d). This suggests that the flow's
623 internal yield strength did not allow down-slope flowage until a minimum shear stress was overcome,
624 similarly to a Bingham-plastic fluid (Furbish, 1987). Assuming that flow density was not much
625 different than deposit density ρ_{dep}, i.e. 1400 kg/m^3 (as it was calculated by considering a known
626 volume of deposits and weighting it), the yield strength τ_0, e.g. the minimum shear stress for the
627 down-slope movement of the debris flow, was evaluated as 700 Pa by means of the
628 relation $\tau_0 = \rho_{dep} g \sin\alpha d$, with α=1.5° as slope angle at deposit freezing and d = 2m as deposit
629 thickness.

630 The stratidfied layer, when cropping out on the gentle slope of the volcano flank, shows a thickness
631 of 0.5 m; whereas, when it occurs along the steeper slopes of the gullies departing from the crater
632 rim, is split into two parts by the intercalated massive layer of the underflow, resulting in a 0.15 m
633 thick basal part (Fig. 14e) and a 0.35 m thick top part (Fig. 14f). It exhibits small dunes of lapilli and
634 ash of 1 m wavelegth and 0.1 m in height (Fig. 14e). The intercalated massive layer is 1.6 m thick.
635 Such interpenetrating stratigraphy between the massive and the tractional layer, which can be
636 followed along the gullies, can be explained by the different speed of the two flows. The dilute current
637 overtook the slower basal flow, initiating sedimentation of the tractional layer. After the massive flow
638 passed over, the aggradation of the tractional layer continued as long as the current was fed from the
639 source. Lots of examples of such a kind of stratigraphy are reported for turbidites and debris flows
640 (Talling et al., 2004). Basing on the assumption that the underflow and the overcurrent were formed
641 almost contemporaneously by the eruption column impact at the crater rim, the speed of the underflow
642 can be estimated by dividing the distance from the crater rim by the total time the underflow took to
643 reach the tractive layer at the "split" location. The total time was obtained by summing up the time
644 that the overcurrent took to reach the "split" location, and the time that the overcurrent took to form,
645 by aggradation, the stratified layer found under the massive one, which is 0.15 m thick. The former
646 time, 52 s, was calculated by the distance, 1.6 km, divided by the height integrated average speed of
647 the overcurrent, ca. 30 ms^{-1}. The average speed of the overcurrent was calculated by means of the
648 turbulent boundary layer shear flow approximation $\overline{u(H)} = u_* \left({}^{1}/_{k} ln {}^{H}/_{k_s} + 6 \right)$, where k_s is ground
649 roughness measured as 0.5 m in the field (as resulted from averaging the height of roughness elements
650 of the substrate) and $\overline{u(H)}$ is the height integrated average speed. u_* and H were obtained by data of
651 Mele et al. (2011), see Tab. 2. The time of aggradation of the stratified layer found under the massive
652 layer, 375 s, resulted from $d/S_r/\rho_{dep}$, where S_r is the sedimentation rate of the dilute overcurrent at
653 the "split" location. Step by step calculation of S_r of the vercurrent is found in the supporting file G.
654 The total time that the underflow took to reach the split location was 428 s, corresponding in a height-

averaged velocity of the massive undercurrent of 3.7 m/s, which is much slower than the that of the overcurrent (about 30 m/s) as it is expected for a highly concentrated debris flow moving downslope. By inverting the equation of the height-averaged velocity of a Bingham-plastic fluid:

$$\overline{u}(y) = d\left(\frac{\rho g sin\alpha d}{3\mu} - \frac{\tau_0}{2\mu}\right) \quad (19)$$

and using in Equation (19) the yield strength τ_0 previously obtained, the thickness d of the massive layer and a slope angle at the "split" location of 6.5°, a viscosity μ of 200 Pas is obtained, which completes the rheological characterization of the massive underflow. Such a rheology is compatible with that of sedimentary debris flows, to which massive pyroclastic flows have been sometimes compared in the literature (Fink et al., 1981; Major and Pierson, 1992; Major and Iverson, 1999; Palladino and Valentine, 1995; Capra et al., 2018). While such flows maintain mobility only inside channels and stop at the gully apron, where the slope abruptly decreases, still they are highly hazardous in the proximal zones at the foot of the volcano, because of the high mass load, thickness and temperature, that render them highly destructive.

Q_b and S_{rw} were calculated for the stratified layer of Mercato cropping below the massive one (fig. 14e). Equations (5) and (10) were used for the calculation of Q_b, with a resulting value 0.011 m^2s^{-1}. Equation (14) was used for the calculation of S_r. As input, data from Mele et al. (2011) were used, see Tab. 2. By means of Equations (7) and (12) S_r was transformed into S_{rw} with a value of 0.0004 m^2s^{-1}. With these values of Q_b and S_{rw} the layer with small-dune bedforms of Mercato plots, in the diagram of Fig. 10, in the field of stratified deposits, with a lower value of S_{rw}/Q_b when compared to experimental deposits. The lapilli and ash small-dune structures of Mercato stratified deposit, with a wavelength about 1 m, and a thickness of about 0.1m (Fig. 14e) further confirm, by the position on the diagram, the inverse relationship between S_{rw}/Q_b and bedform scale.

6. Summary and conclusion

679 The present paper aims at defining the threshold ratio of the sedimentation and bedload transportation
680 rates that marks the limit between the formation of massive vs stratified deposits by suspension
681 currents. By the result of experiments, the threshold ratio was set at S_{rw}/Q_b =100. The same ratio
682 separates structureless fine-ash beds from layers with shear structures. By the experiments it was
683 demonstrated that, in the range of tested fluid dynamics, fine ash never shows shear structures. It is
684 in fact difficult to move by traction very fine material that exposes a limited surface to the basal shear
685 stress of a current.
686 The paucity, in the literature, of data of the kind of those proposed here depends on the relatively few
687 experiments on deposition from suspension currents. Such experiments need a scale and equipment
688 quite different from those of the more frequently designed "flume" type, which generally do not
689 include the contemporaneous measurement of suspension sedimentation and bedload transportation.
690 For the same reason, the experiments carried out in this paper, due to the time length of design,
691 construction, execution, analysis and post processing, cannot be repeated multiple times, in the life
692 span of a research-project, as to cover the complete range of eruption conditions leading to the
693 formation of pyroclastic deposits. A comparison with the natural cases shows that the main physical
694 parameters of experiments are in the same order of magnitude of real pyroclastic density currents and
695 that the facies model of the experimental deposits of Fig. 8 is similar to what has been reported for
696 some ignimbrites, including the deposits of the Agnano Monte-Spina eruption of Campi Flegrei
697 studied in this paper. The facies model could be of help in the interpretation of the lateral facies
698 architecture of pyroclastic density currents deposits.
699 The S_{rw}/Q_b ratio has been calculated also for natural deposits of Campi Flegrei and Vesuvius, which
700 were plotted in the diagram of Fig. 10. The diagram was able to correctly discriminate between
701 massive and stratified deposits, legitimating the scaling between experimental and natural deposits.
702 The deposits with shear structures of the Mercato eruption at Vesuvius and of the Sbirri and Verdolino
703 localities at Campi Flegrei plot, on Fig. 10, in the field of stratified deposits with lower S_{rw}/Q_b values
704 with respect to the experimental deposits, and allow to extend the range of structures covered in the

diagram. Starting from the smaller ripple-like structures and, by gradually increasing bedform wavelength and height, going up to deposits with small dunes, the larger are the structures, the lower is the S_{rw}/Q_b value, with a regular decrease at increasing bedform scale. This may suggest that it happens in natural deposits, as it happens in the experimental ones, that the scale of bedforms is inversely related to S_{rw}/Q_b.

The application of the classificatory diagram to natural deposits demonstrated also the potentiality in the reconstruction of physical characteristics of the eruptions, which have major implications on hazard assessment. Application to the proximal facies of B2 deposits of Campi Flegrei represents a new way of reconstructing *MER* feeding the pyroclastic density currents of past eruptions.

Application to the distal fine-ash deposits of Campi Flegrei allowed the determination, by means of the threshold limit between massive vs tractional sedimentation, of the duration of passage of the unbreathable current in distal localities, which could last for almost an hour in the case of the Agnano Monte-Spina eruption.

Application to the deposits of the Mercato eruption of Vesuvius, has helped demonstrating that the eruptive column can lead to the formation of both a slow, concentrated, underflow and a dilute overcurrent. It has been demonstrated that the underflow behaves as a debris flow, controlled by a Bingham rheology with a yield strength of 700 Pa and viscosity of 200 Pas, and moves at a few meters per second, independent from the dilute, faster, overcurrent.

It is reasonable to hypothesize that the numerical limits of the discriminatory diagram of Fig. 10 would likely be more precisely defined by additional applications to a larger number of pyroclastic deposits, with the aim to also further extend the range up to larger-scale dunes of more intense pyroclastic density currents. Further applications of the diagram could also prove whether it can be of some use also in the study of other density currents as, for example, turbiditic currents.

Acknowledgement.

The manuscript took a great advantage by the thorough revision of Jaco H. Baas, Mike Clare and Martin Jutzeler. Roberto Isaia is Acknowledged for the fruitful discussion during the field work at Campi Flegrei. Roberto Sulpizio is Acknowledged for the fruitful discussion during the field work at Vesuvius.

References

Ashley, G.M. (1990) Classification of large-scale subaqueous bedforms: a new look at an old problem; SEPM bedforms and bedding structures. J. Sediment. Petrol., **60**(1), 160-172.

Baas, J.H., Best, J.L. and **Peakall, J.** (2011) Depositional processes, bedform development and hybrid bed formation in rapidly decelerated cohesive (mud–sand) sediment flows. Sedimentology, **58**(7), 1953-1987.

Baxter, P.J., Boyle, R., Cole, P., Neri, A., Spence, R.S. and **Zuccaro, G.** (2005) The impacts of pyroclastic surges on buildings at the eruption of the Soufrière Hills volcano, Montserrat. Bull. Volcanol., **67**, 292–313.

Branney, M.J. and **Kokelaar, B.P.** (1997) Giant bed from a sustained catastrophic density current flowing over topography: Acatlán ignimbrite, Mexico. Geology, **25**, 115–118.

Branney, M.J. and **Kokelaar, P.** (2002) Pyroclastic Density Currents and the Sedimentation of Ignimbrites. Geological Society, London, Memoirs, 27 pp.

Breard, E.C., Lube, G., Jones, J.R., Dufek, J., Cronin, S.J., Valentine, G.A. and **Moebis, A.** (2016) Coupling of turbulent and non-turbulent flow regimes within pyroclastic density currents. Nat. Geosci., **9**(10), 767-771.

Breard, E.C.P. and **Lube, G.** (2017) Inside pyroclastic density currents – uncovering the enigmatic flow structure and transport behaviour in large-scale experiments. Earth Planet. Sci. Lett., **458**, 22-36.

Brown, R.J. and **Branney, M.J.** (2013) Internal flow variations and diachronous sedimentation within extensive, sustained, density stratified pyroclastic density currents down gentle slopes, as revealed by the internal architectures of ignimbrites in Tewnerife. Bull. Volcanol., **75**, 1–24.

Bursik, M.I. and **Woods, A.W.** (1996) The dynamics and thermodynamics of large ash flows. Bull. Volcanol. **58**, 175–193.

Capra, L., Sulpizio, R., Márquez-Ramirez, V.H., Coviello, V., Doronzo, D.M., Arambula-Mendoza, R. and **Cruz, S.** (2018) The anatomy of a pyroclastic density current: the 10 July 2015 event at Volcán de Colima (Mexico). Bull. Volcanol., **80**, 34.

Caricchi, L., Vona, A., Corrado, S., Giordano, G. and **Romano, C.** (2014) 79 AD Vesuvius PDC deposits' temperatures inferred from optical analysis on woods charred in-situ in the Villa dei Papiri at Herculaneum (Italy). J. Volcanol. Geotherm. Res., **289**, 14–25.

Cartigny, M.J.B., Ventra, D., Postma, G. and **van Den Berg, J.H.** (2014) Morphodynamics and sedimentary structures of bedforms under supercritical-flow conditions: New insights from flume experiments. Sedimentology, **61**, 712-748.

Chanson, H. (2009) Current knowledge in hydraulic jump and related phenomena. A survey of experimental results. Eur. J. Mech., **28**, 191–210.

Cioni, R., Marianelli, P., Santacroce, R. and **Sbrana, A.** (2000) Plinian and subplinian eruptions. In: Sigurdsson H (ed) Encyclopedia of volcanoes. Academic, New York, 477–494 pp.

Crowe, B.M. and **Fisher, R.V.** (1973) Sedimentary Structures in Base-Surge Deposits with Special Reference to Cross-Bedding, Ubehebe Craters, Death Valley, California. Geol. Soc. Am. Bull. **84**(2), 663-682.

Dade, W. B. (2003) The emplacement of low-aspect ratio ignimbrites by turbulent parent flows, J. Geophys. Res., **108**(B4), 2211.

Dartevelle, S., Ernst, G.G.J., Stix, J. and **Bernard, A.** (2002) Origin of the Mount Pinatubo climactic eruption cloud: implications for volcanic hazards and atmospheric impacts. Geology, **30** (7), 663–666.

de Vita, S., Orsi, G., Civetta, L., Carandente, A., D'Antonio, M., Di Cesare, T., Di Vito, M.A., Fisher, R.V., Isaia, R., Marotta, E., Ort, M., Pappalardo, L. and **Southon, J.** (1999) The Agnano-

799 Monte Spina eruption in the densely populated, restless Campi Flegrei caldera (Italy). J. Volcanol.
800 Geotherm. Res. **91**, 269–301.
801
802 **Dell'Erba F.** (2004) Definizione di parametrici fisici di alcune eruzioni esplosive della caldera dei
803 Campi Flegrei negli ultimi 15 ka: implicazioni per la valutazione della pericolosità vulcanica. Ph.D.
804 thesis, Bari, University of Bari, 147 pp.
805
806 **Dellino, P., Mele, D., Bonasia, R., Braia, G., La Volpe, L. and Sulpizio, R.** (2005) The analysis of
807 the influence of pumice shape on its terminal velocity. Geophys. Res. Lett., **32**, L21306.
808
809 **Dellino, P., Zimanowski, B., Büttner, R., La Volpe, L.** and **Sulpizio, R.** (2007) Large-scale
810 experiments on the mechanics of pyroclastic flows: design, engineering, and first results. J. Geophys.
811 Res., **112**, B04202.
812
813 **Dellino, P., Mele, D., Sulpizio, R., La Volpe, L.** and **Braia, G.** (2008) A method for the calculation
814 of the impact parameters of dilute pyroclastic density currents based on deposits particle
815 characteristics. J. Geophys. Res. **113**, B07206.
816
817 **Dellino, P., Dioguardi, F., Zimanowski, B., Büttner, R., Mele, D., La Volpe, L., Sulpizio, R.,**
818 **Doronzo, D.M., Sonder, I., Bonasia, R., Calvari, S.** and **Marotta, E.** (2010a) Conduit flow
819 experiments help constraining the regime of explosive eruptions. J. Geophys. Res., **115**, B04204.
820
821 **Dellino, P., Büttner, R., Dioguardi, F., Doronzo, D.M., La Volpe, L., Mele, D., Sonder, I.,**
822 **Sulpizio, R.** and **Zimanowski, B.** (2010b) Experimental evidence links volcanic particle
823 characteristics to pyroclastic flow hazard, Earth Planet. Sci. Lett., **295**, 314–320.
824

825 **Dellino, P., Dioguardi, F., Mele, D., D'Addabbo, M., Zimanowski, B., Büttner, R., Doronzo,**
826 **D.M., Sonder, I., Sulpizio, R., Dürig, T. and La Volpe, L.** (2014) Volcanic jets, plumes, and
827 collapsing fountains: evidence from large-scale experiments, with particular emphasis on the
828 entrainment rate. Bull. Volcanol., **76**, 834.

829 **Dellino P., Dioguardi F., Doronzo D.M.** and **Mele D.** (2019) The rate of sedimentation from
830 turbulent suspension: An experimental model with application to pyroclastic density currents and
831 discussion on the grain-size dependence of flow runout. Sedimentology, **66**(1), 129-145.

832

833 **Dioguardi, F., Dellino, P.** and **de Lorenzo, S.** (2013) Integration of large-scale experiments and
834 numerical simulations for the calibration of friction laws in volcanic conduit flows. J. Volcanol.
835 Geotherm. Res., **76**(6), 75-90.
836
837 **Dioguardi, F.** and **Dellino, P.** (2014) PYFLOW: A computer code for the calculation of the impact
838 parameters of Dilute Pyroclastic Density Currents (DPDC) based on field data. Comput. Geosci., **66**,
839 200-210.
840
841 **Dioguardi, F.** and **Mele, D.** (2018) PYFLOW_2.0: a computer program for calculating flow
842 properties and impact parameters of past dilute pyroclastic density currents based on field data. Bull.
843 Volcanol., **80**, 28.
844
845 **Dioguardi, F., Mele, D**. and **Dellino, P.** (2018) A New One-Equation Model of Fluid Drag for
846 Irregularly Shaped Particles Valid Over a Wide Range of Reynolds Number. J. Geophys. Res., **123**,
847 144-156.
848

849 **Druitt, T.H.** (1992) Emplacement of the 18 May1980 lateral blast deposit ENE of Mount St. Helens,
850 Washington. Bull. Volcanol., **54**(7), 554-572.
851
852 **Druitt, T.H.** and **Kokelaar, B.P.** (2002) The eruption of Soufrière Hills Volcano, Montserrat, from
853 1995 to 1999. Geol. Soc. Lond. Mem. **21**.
854
855 **Dufek, J.** (2016) The fluidmechanics of pyroclastic density currents. Annu. Rev. Fluid. Mech., **48**(1),
856 459-485.
857
858 **Duller, R.A., Mountney N.P., Russel, A.J.** and **Cassidy, N.C. (2008)** Architectural analysis of a
859 volcaniclastic jökulhlaup deposit, southern Iceland: sedimentary evidence for supercritical flow.
860 Sedimentology, **55**(4), 939-964.
861
862 **Esposti Ongaro, T., Orsucci, S.** and **Cornolti, F.** (2016) A fast, calibrated model for pyoclastic
863 density currents kinematics and hazard. J. Volcanol Geotherm. Res., **327**, 257-272.
864
865 **Fink, J.H., Malin, M.C., D'Alli, R.E.** and **Greeley, R.** (1981) Rheological properties of mudflows
866 associated with the spring 1980 eruptions of Mount St. Helens Volcano Washington. Geophys. Res.
867 Lett., **8**(1),43-36.
868
869 **Fisher, R.V.** (1979) Models for pyroclastic surges and pyroclastic flows. Journal of Volcanology
870 and Geothermal Research., **6**, 305-318.
871
872 **Fisher, R.V.** (1990) Transport and deposition of a pyroclastic surge across an area of high relief: the

873 18 May 1980 eruption of Mount St. Helens, Washington. Geol. Soc. Am. Bull., **102**, 1038–1054.
874
875 **Furbish, D.J.** (1997) Fluid Physics in Geology. Oxford University Press, New York, Oxford.
876 **476 pp.**
877
878 **Gernon, T.M., Upton, B.G.J.,** and **Hincks, T.K.** (2013) Eruptive history of an alkali basaltic
879 diatreme from Elie Ness, Fife, Scotland. Bull. Volcanol., **75**, 704.
880
881 **Gladstone, C., Phillips, J.C.** and **Sparks, R.S.J.** (1998) Experiments on bidisperse, constant-volume
882 gravity currents: propagation and sediment deposition. Sedimentology, **45**, 833–843.
883
884 **Jutzeler, M., McPhie, J., Allen, S.R. and Proussevitch, A.A.** (2015) Grain-size distribution of
885 volcaniclastic rocks 2: Characterizing grain size and hydraulic sorting. Journal of Volcanology and
886 Geothermal Research, **301**, 191-203.
887
888 **Kneller, B.C.** and **Branney, M.J.** (1995) Sustained high-density turbidity currents and the deposition
889 of thick massive sands. Sedimentology, **42**, 607–616.
890
891 **Kok, J.F., Parteli, E.J.R., Michaels, T.I.** and **Karam, D.B.** (2012) The physics of windblown sand
892 and dust. Rep. Prog. Phys., **75**, 1–72.
893
894 **Kokelaar, P., Raine, P.** and **Branney, M.J.** (2007) Incursion of a large-volume, spatter-bearing
895 pyroclastic density current into a caldera lake: Pavey Ark ignimbrite, Scafell Caldera, England. Bull.
896 Volcanol., **70**, 23–54.
897

Lajoie, J., Boudon, G. and **Bourdier, J.L.** (1989) Depositional mechanics of the 1902 pyroclastic nuée ardente deposits of Mt. Pelée, Martinique. J. Volcanol. Geotherm. Res., **38**, 131–142.

Lowe, D.R. (1982) Sedimentary gravity flows: II. Depositional models with special reference to the deposits of high density turbidity currents. J. Sediment. Petrol., **52**, 279–297.

Lowe, D.R. (1988) Suspended-load fallout rate an independent variable in the analysis of current structures. Sedimentology, **35**(5), 765-776.

Lube, G., Breard, E.C.P., Cronin, S.J. and **Jones, J.** (2015) Synthesizing large-scale pyroclastic flows: experimental design, scaling, and first results from PELE. J. Geophys. Res. Solid Earth. **120**(3), 1487–1502.

Major, J. J., and **Pierson, T. C.** (1992) Debris flow rheology: Experimental analysis of fine-grained slurries, Water Resour. Res., **28**, 841–857.

Major, J. J., and **Iverson R. M.** (1999) Debris-flow deposition—Effects of pore-fluid pressure and friction concentrated at flow margins, Geol. Soc. Am. Bull., **111**, 1424–1434.

Manning, A.J. and **Schoellhamer, D.H.** (2013) Factors controlling floc settling velocity along a longitudinal estuarine transect. Mar. Geol., **345**, 266-280.

Manville, V., Segschneider, B., Newton, E., White, J.D.L., Houghton, B.F. and **Wilson, C.J.N.** (2009) Environmental impact of the 1.8 ka Taupo eruption, New Zealand: landscape responses to a large-scale explosive rhyolite eruption. Sediment. Geol., **220**, 318–336.

Meiburg, E. and **Kneller, B.C.** (2010) Turbidity currents and their deposits. Annu. Rev. Fluid Mech., **42**, 135–156.

Mele, D., Sulpizio, R., Dellino, P. and **La Volpe, L.** (2011) Stratigraphy and eruptive dynamics of a pulsating Plinian eruption of Somma-Vesuvius: the Pomici di Mercato (8900 years B.P.). Bull. Volcanol., **73**, 257–278.

Mele, D., Dioguardi, F., Dellino, P., Isaia, R., Sulpizio, R. and **Braia, G.** (2015) Hazard of pyroclastic density currents at the Campi Flegrei Caldera (Southern Italy) as deduced from the combined use of facies architecture, physical modeling and statistics of the impact parameters. J. Volcanol. Geotherm. Res., **299**, 35–53.

Middleton, G.V. and **Southard, J.B.** (1984) Mechanics of Sediment Movement, 2nd edn. Society of Economic Paleonologists and Mineralogists, Tulsa, OK, 401 pp.

Miller, M.C., McCave, I.N. and **Komar, P.D.** (1977) Threshold of sediment motion under unidirectional currents. Sedimentology, **24**(4), 507–527.

Palladino, D.M. and **Valentine, G.A.** (1995) Coarse-tail vertical and lateral grading in pyroclastic flow deposits of the Latera Volcanic Complex (Vulsini, Central Italy): origin and implications for flow dynamics. J. Volcanol. Geotherm. Res., **69**, 343–364.

Postma, G., Cartigny, M. and **Kleverlaan, K.** (2009) Structureless, coarse-tail graded Bouma Ta formed by internal hydraulic jump of the turbidity current. Sediment. Geol., **219**, 1–6.

Pritchard, D. and **Gladstone, C.** (2009) Reversing buoyancy in turbidity currents: developing a

hypothesis for flow transformation and for deposit facies and architecture. Mar. Petroleum Geol., **26**, 1997–2010.

Roche, O., Phillips, J.C. and **Kelfoun, K.** (2013) Pyroclastic density currents. In: Fagents, S.A., Gregg, T.K.P., Lopes, R.M.C. (Eds.), Modeling Volcanic Processes: The Physics and Mathematics of Volcanism. Cambridge University Press, pp. 203–229.

Roche, O. (2015) Nature and velocity of pyroclastic density currents inferred from models of entrainment of substrate lithic clasts. Earth Planet. Sci. Lett., **418**, 115–125.

Rowley, P.J., Roche, O., Druitt. T.H. and **Car, R.** (2014) Experimental study of dense pyroclastic density currents using sustained, gas-fluidized granular flows. Bull.Volcanol., **76**, 855.

Sparks, R.S.J. (1976) Grain size variations in ignimbrites and implications for the transport of pyroclastic flows. Sedimentology, **23**(2), 147-188.

Sulpizio, R., Mele, D., Dellino, P. and **La Volpe, L.** (2007) Deposits and physical properties of pyroclastic density currents during complex Subplinian eruptions: the AD 472 (Pollena) eruption of Somma-Vesuvius, Italy. Sedimentology, **54**, 607–635.

Sulpizio, R. and **Dellino, P.** (2008) Sedimentology, depositional mechanisms and pulsating behavior of pyroclastic density currents. In: Calderas Volcanism: Analysis, Modelling and Response, vol. 10, Developments in Volcanology, (Eds. J. Mart_ı and J. Gottsman), pp. 57–96. Elsevier, Amsterdam.

Sulpizio, R., Dellino, P., Doronzo, D.M. and **Sarocchi, D.** (2014) Pyroclastic density currents: state of the art and perspectives. J. Volcanol. Geotherm. Res., **283**, 36–65.

Sumner, E.J., Amy, L.A. and **Talling, P.J.** (2008) Deposit structure and processes of sand deposition from decelerating sediment suspensions. J. Sediment. Res., **78**(8), 529-547

Talling, P.J., Amy, L.A., Wynn, R.B., Peakall, J. and Robinson, M. (2004) Beds comprising debrite sandwiched within co-genetic turbidite: Origin and widespread occurrence in distal depositional environments. Sedimentology, **51**, 163-194.

Valentine, G. A. (1998) Damage to structures by pyroclastic flows and surges, inferred from nuclear weapons effects, J. Volcanol. Geotherm. Res., **87**, 117–140.

Vazquez, J.A. and **Ort, M.H.** (2006) Facies variation of eruption units produced by the passage of single pyroclastic surge currents, Hopi Buttes volcanic field, USA. J. Volcanol. Geotherm. Res., **154**, 222–236.

Wilcock, P.R. and **Crowe, J.C.** (2003) Surface-based transport model for mixed-size sediment: J. Hydraul. Eng., **129**, 120-128.

Woods, A.W., Sparks, R.S.J., Ritchie, L.J., Batey, J., Gladstone, C. and **Bursik M.I.** (2002) The explosive decompression of a pressurized volcanic dome: the 26 December 1997 collapse and explosion of Soufrière Hills Volcano, Montserrat. Geol. Soc. Lond. Mem., **21**(1), 457:465.

998 **Wright, J.V., Smith A.L., Roobol, M.J., Mattioli, G.S.** and **Fryxell, J.E.** (2016) Distal ash
999 hurricane (pyroclastic density current) deposits from a ca. 2000 yr B.P. Plinian-style eruption of
1000 Mount Pelée, Martinique: Distribution, grain-size characteristics, and implications for future hazard.
1001 GSA Bull., **128**, 777-791.
1002

1003 **Xu, D., Bai, Y., Ji, C.** and **Williams J.** (2015) Experimental study of the density influence on the
1004 incipient motion and erosion modes of muds in unidirectional flows: the case of Huangmaohai
1005 Estuary. Ocean Dyn., **59**, 751-763.
1006

1007 **Zanke, U.C.E.** (2001) On the physics of flow-driven sediments (bed-load). Int. J. Sediment Res.,
1008 **16**(1), 1-18.
1009

1010 **Figure captions**
1011

1012 Fig. 1. Sketch design of the experimental apparatus with description of the main parts. Modified after
1013 Dellino et al., 2019. A: Packs of interconnected compressed-gas bottles. B:hub connecting the hoses
1014 to the base plate of the conduit. C: the conduit.
1015

1016 Fig. 2. Grain-size distribution of the material used for experiments. The size is expressed in ϕ units
1017 ($\phi=-log_2 D$, where D is size in mm). The relative fractions of components are shown. The xx symbol
1018 means crystals. A: multicomponent grain-size distribution of the coarse material coming from the
1019 Veusvius composition. B: grain-size distribution of the fine glassy material coming from the Campi
1020 Flegrei composition. Modified after Dellino et al., 2019.
1021
1022

Fig. 3. On the left, a photo showing the passage of an experimental current, with values of average velocity u_{avg}, shear velocity, u_*, thickness and dynamics pressure in the inset. On the wright, the sensor network recording pressure.

Fig. 4. General view of deposit dispersal area with traces of the sampling areas.

Fig. 5. Display mount showing phases of the experiment and massive deposits. A: formation of the dense gas-particle foutain at the conduit exit. B: Collapse of the fountain and impact on the ground. C: The massive deposit formed by an experiment fed with the coarse grain size at the centre of the impact. The lateral undulations (marked by arrows) formed by the incipient shear at the lateral zone of the impact are visible. D: Cuttings showing the internal sections of the massive deposit. The field of view is 0.5 m across. E. A massive deposit formed at the centre of the impact of an experiment fed with the fine material. F: The structureless deposit formed by an experiment fed with the fine grain size.

Fig. 6. Display mount showing the fully turbulent density current and deposits structures. A: the density current fed from the fountain collapse. B: widely spaced coarse ash cm thick ripple-like structures. The field of view is 1m across. C: close up view of the passage of a density current showing the shearing effect on the particles at the base. D: close up view of the successive frame of figure 6c with continuing shear of particles at the base of the current. E: Narrowly spaced coarse ash cm thick ripple-like structures. F: widely spaced mm thick medium ash ripple-like structures.

Fig. 7. Far reaches of the current. A: end of the fountain feeding a current, resulting in washload transportation. B: the submillimetric veil of ash representing the washload.

Fig. 8. Sketch of fountain/current evolution along runout with the lateral facies evolution of deposits.

Fig. 9. Diagram showing the functional relationship of the ratio between the concentration in the fountain and that in the suspension current (*C1/C2*) against the ratio of normalized bedload transportation and total fallout rate (Q_b*/S_{fr}). The equation of the best-fit law interpolating data, and the correlation coefficient, are inset.

Fig. 10. S_{rw} - Q_b discrimination diagram between massive and stratified deposits. The separation line between massive and stratified deposits is set at the threshold of $S_{rw}=100Q_b$. Both the experimental and natural deposits are plot. The relationship between structures spacing and S_{fr}/Q_b is shown. The dashed line ($S_{fr}=4Q_b$) represents the limit between narrowly spaced and widely spaced ripple like structures of the experimental deposits. FAMass = Fine ash massive deposit; LAMass = Lapilli and ash massive deposit; CARip.narr = Coarse Ash narrowly spaced ripple-like structures; CARip.wide = Coarse ash widely spaced ripple like structures; MARip.wide = Medium Ash widely spaced ripple-like structures; LASmDune = Lapilli and Ash small dune; FAStrless = Fine Ash structureless beds.

Fig. 11. Digital elevation model, rendered as shaded relief, with illumination from the North of Vesuvius volcano and Campi Flegrei caldera in southern Italy.

Fig.12. Display mount showing the Agnano Monte-Spina B2 deposits used as a model application. A: Digital Elevation Model map showing the Campi Flegrei caldera and the location of deposits. B: A massive deposit with alignments of coarse clasts, representing the impact of a gas-parrticle fountain, cropping out at Vallone del Corvo. C: Massive (bottom) and stratified (top) deposits, cropping at Sbirri, formed by the lateral zone of the fountain impact. The small dunes circled in the image have a 2 m spacing and 0.15 m height. D: On top of the hammer B2 deposits at Verdolino showing widely-spaced ripple-like structures (circled). Structure spacing is about 0.5 m and height about 0.05 m. E: The coin points to the fine-ash layer at Camaldoli.

Fig. 13. Diagram showing the relationship between Mass Eruption Rate (MER) and Desimetric Froude number (Fr_0') for the B2 phase of the Agnano Monte-Spina eruption, as obtained by model application. The line intersecting the curve represents the value of MER calculated by the deposit volume data of Dell'Erba (2004).

Fig. 14. Display mount showing the Mercato eruption deposits used as a case study for model application. The hammer used as a scale for field photographs, is 30 cm long. A: Digital Elevation Model map of Vesuvius. The location of deposits are marked, together with the zone of impact of the eruptive fountain. B: the massive layer formed at the impact of the eruptive fountain. C: the stratified layer formed at the bedload of the suspension current. D: the massive deposit emplaced by freezing at the break-in slope. E: the stratified layer at the base of the massive layer at the split location. Small dune structures are circled. Structure spacing is avbout 1 m, height about 0.1 m. F: the stratified layer on top of the massive layer at the split location

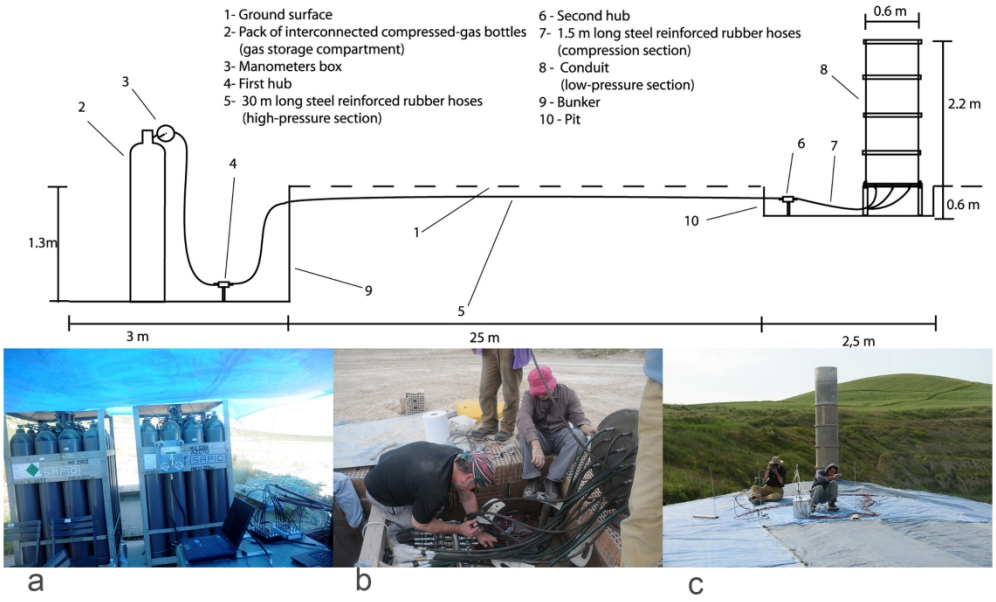

Sketch design of the experimental apparatus with description of the main parts. Modified after Dellino et al., 2019. A: Packs of interconnected compressed-gas bottles. B:hub connecting the hoses to the base plate of the conduit. C: the conduit.

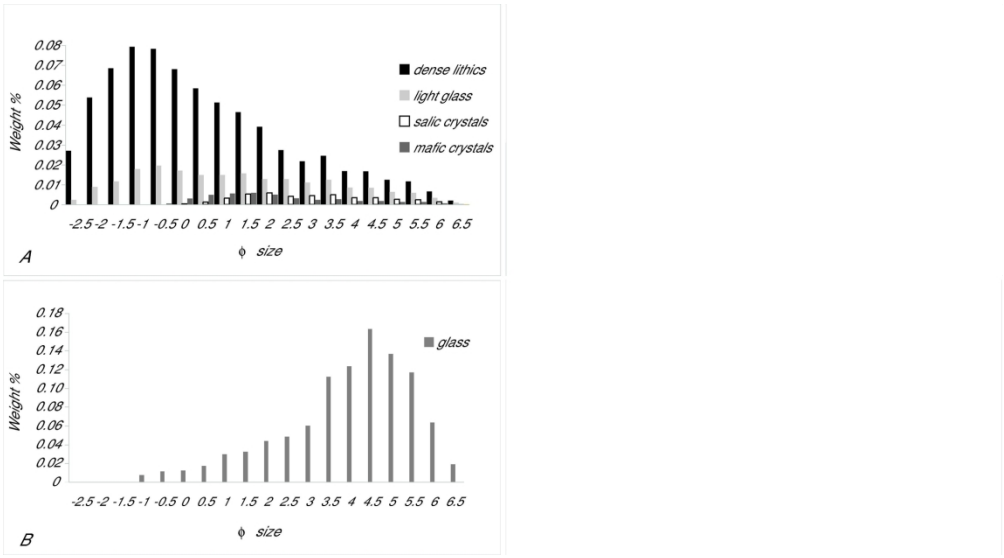

Grain-size distribution of the material used for experiments. The size is expressed in Φ units (Φ=-log2D, where D is size in mm). The relative fractions of components are shown. The xx symbol means crystals. A: multicomponent grain-size distribution of the coarse material coming from the Veusvius composition. B: grain-size distribution of the fine glassy material coming from the Campi Flegrei composition. Modified after Dellino et al., 2019.

185x102mm (300 x 300 DPI)

General view of deposit dispersal area with traces of the sampling areas.

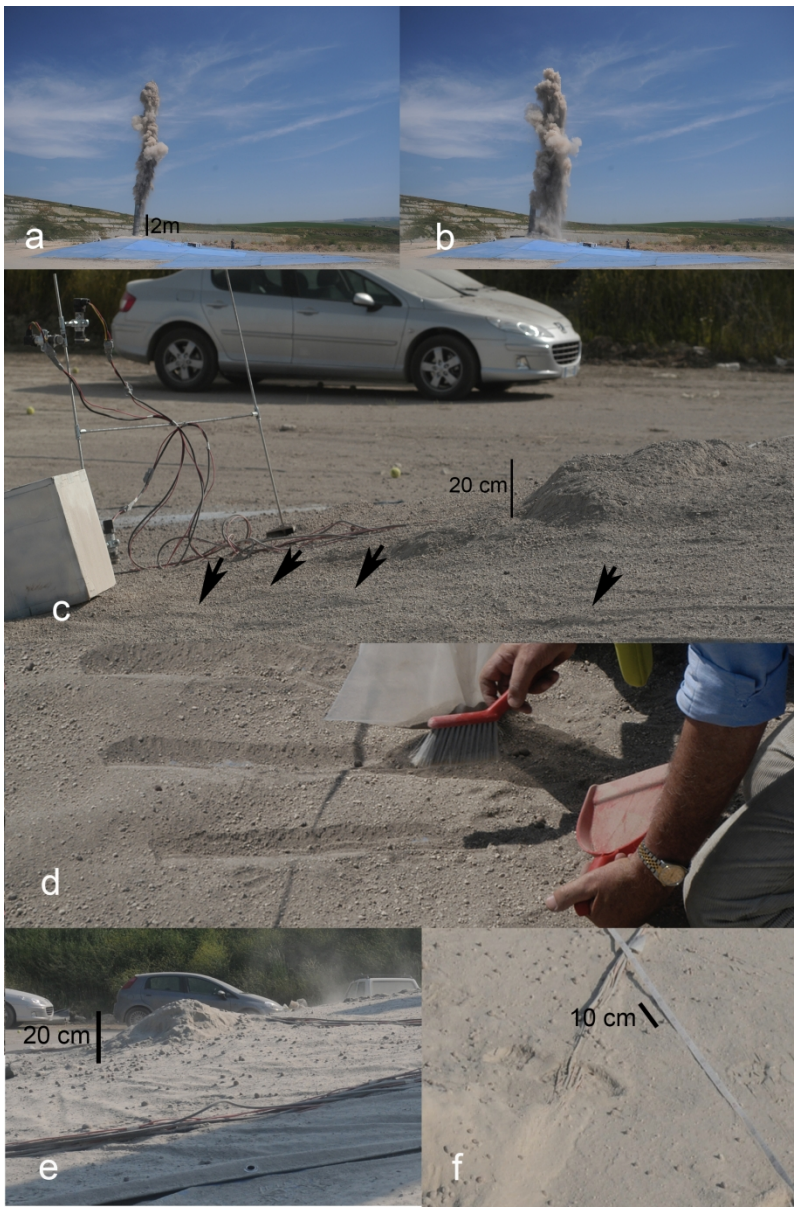

Display mount showing phases of the experiment and massive deposits. A: formation of the dense gas-particle foutain at the conduit exit. B: Collapse of the fountain and impact on the ground. C: The massive deposit formed by an experiment fed with the coarse grain size at the centre of the impact. The lateral undulations (marked by arrows) formed by the incipient shear at the lateral zone of the impact are visible. D: Cuttings showing the internal sections of the massive deposit. The field of view is 0.5 m across. E. A massive deposit formed at the centre of the impact of an experiment fed with the fine material. F: The structureless deposit formed by an experiment fed with the fine grain size.

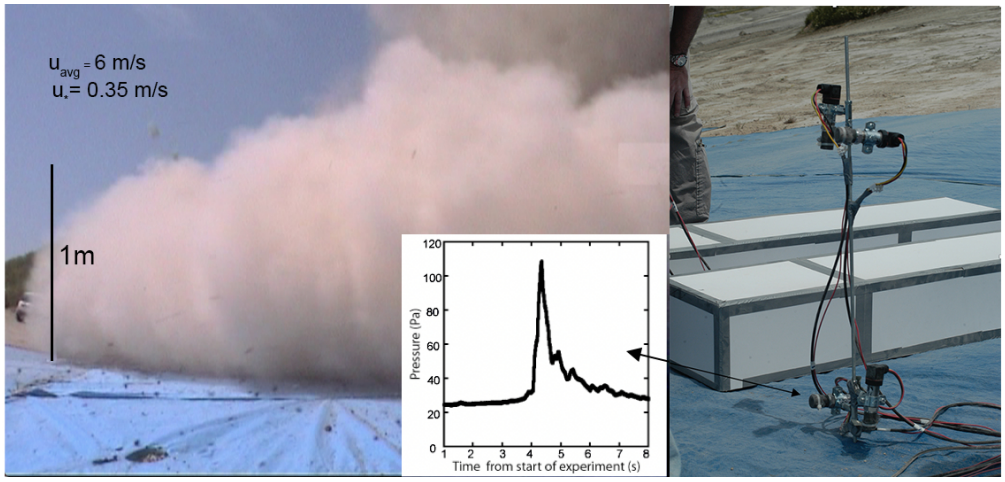

On the left, a photo showing the passage of an experimental current, with values of average velocity uavg, shear velocity, u*, thickness and dynamics pressure in the inset. On the wright, the sensor network recording pressure.

Display mount showing the fully turbulent density current and deposits structures. A: the density current fed from the fountain collapse. B: widely spaced coarse ash cm thick ripple-like structures. The field of view is 1m across. C: close up view of the passage of a density current showing the shearing effect on the particles at the base. D: close up view of the successive frame of figure 6c with continuing shear of particles at the base of the current. E: Narrowly spaced coarse ash cm thick ripple-like structures. F: widely spaced mm thick medium ash ripple-like structures.

Far reaches of the current. A: end of the column feeding a current, resulting in washload transportation. B: the submillimetric veil of ash representing the washload.

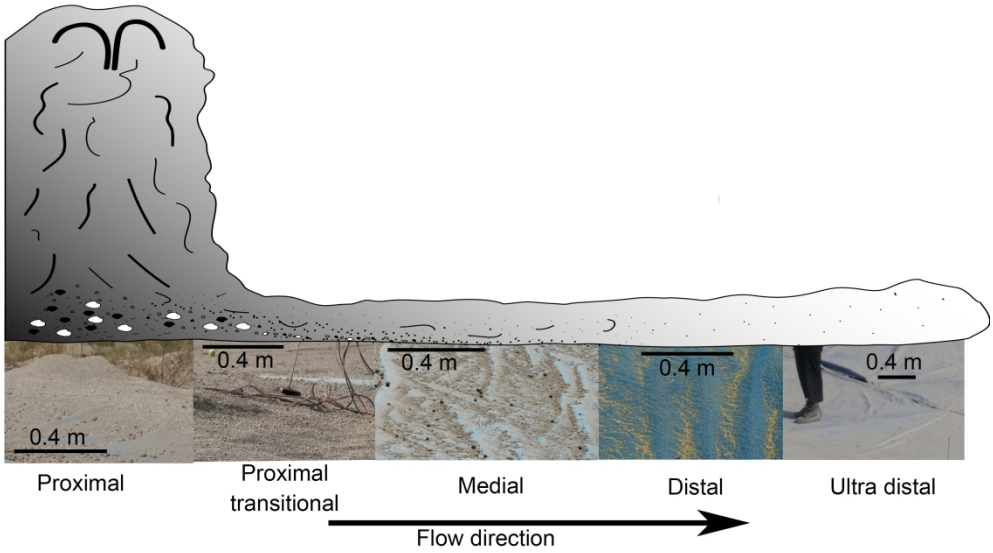

Sketch of column/current evolution along runout with the lateral facies evolution of deposits.

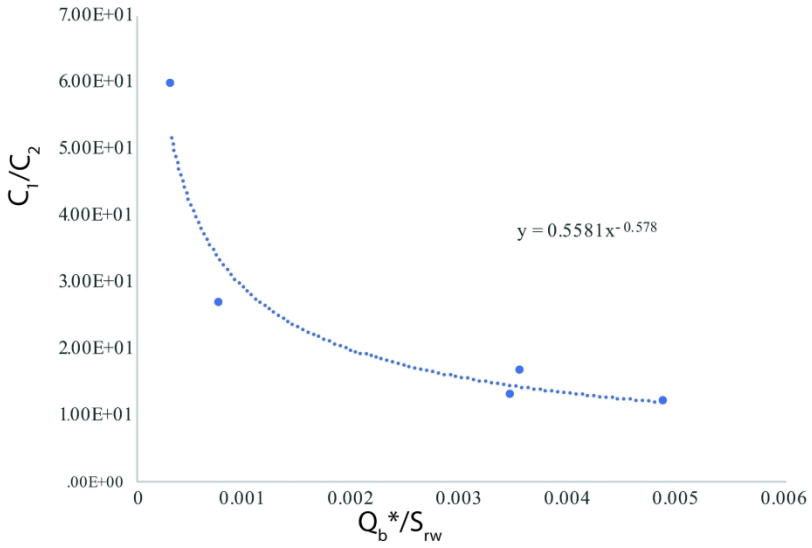

Diagram showing the functional relationship of the ratio between the concentration in the column and that in the suspension current (C1/C2) against the ratio of normalized bedload transportation and total fallout rate (Qb*/Sfr). The equation of the best-fit law interpolating data, and the correlation coefficient, are inset.

219x139mm (300 x 300 DPI)

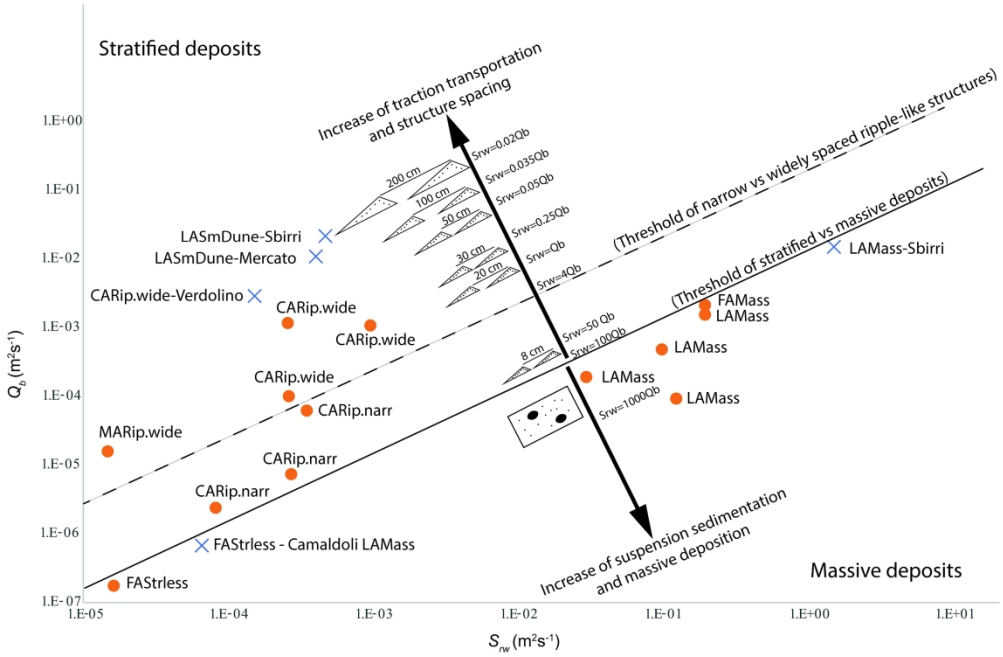

Srw - Qb discriminatory diagram between massive and stratified deposits. The separation line between massive and stratified deposits is set at the threshold of Srw=100Qb. Both the experimental and natural deposits are plot. The relationship between structures spacing and Sfr/Qb is shown. The dashed line (Sfr=4Qb) represents the limit between narrowly spaced and widely spaced ripple-like structures of the experimental deposits. FAMass = Fine-ash massive deposit; LAMass = Lapilli and ash massive deposit; CARip.narr = Coarse Ash narrowly spaced ripple-like structures; CARip.wide = Coarse ash widely spaced ripple like structures; MARip.wide = Medium Ash widely spaced ripple-like structures; LASmDune = Lapilli and Ash small dune; FAStrless = Fine Ash structureless beds.

294x206mm (300 x 300 DPI)

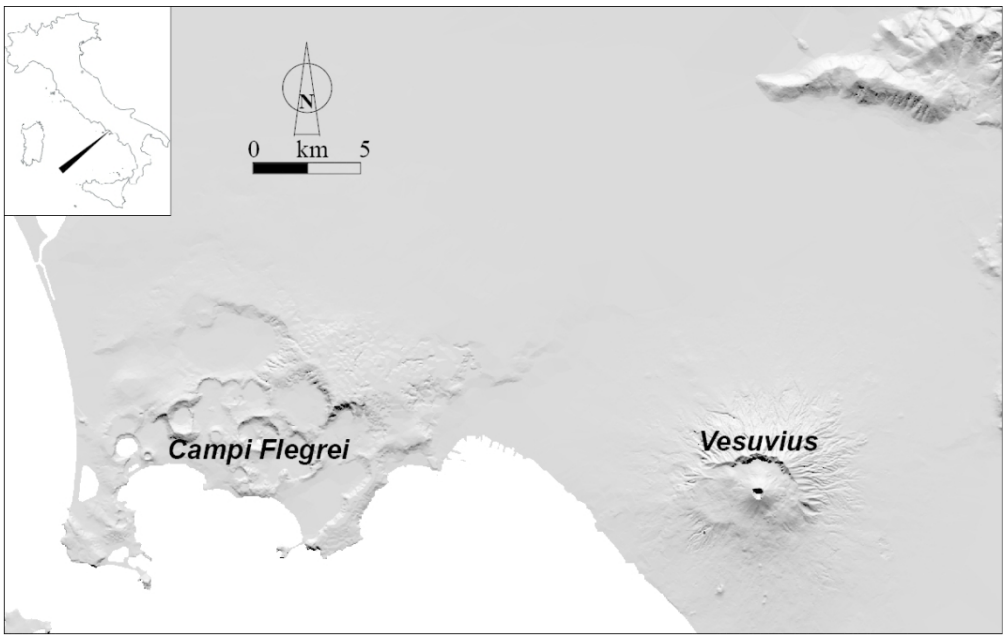

Digital elevation model, rendered as shaded relief, with illumination from the North of Vesuvius volcano and Campi Flegrei caldera in southern Italy.

102x64mm (300 x 300 DPI)

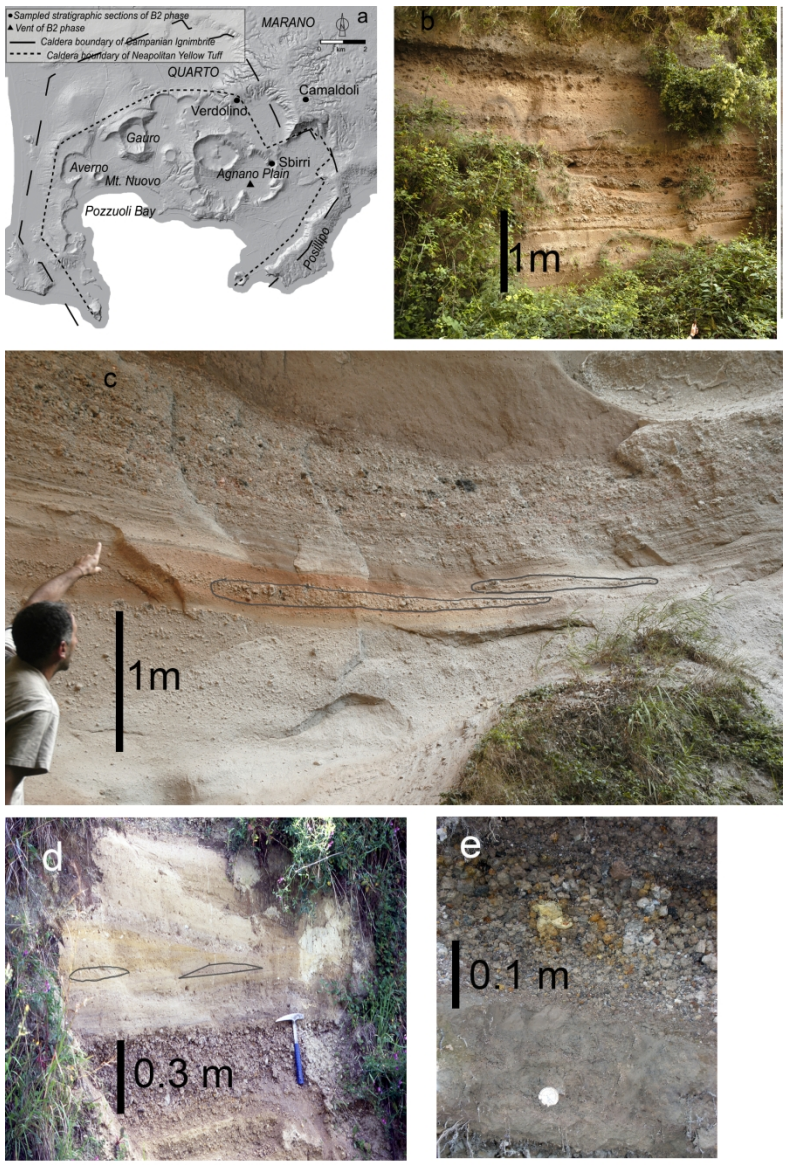

Display mount showing the Agnano Monte-Spina B2 deposits used as an application. A: Digital Elevation Model map showing the Campi Flegrei caldera and the location of deposits. B: A massive deposit with alignments of coarse clasts, representing the impact of a gas-particle column, cropping out at Vallone del Corvo. C: Massive (bottom) and stratified (top) deposits, cropping at Sbirri, formed by the lateral zone of the fountain impact. The small dunes circled in the image have a 2 m spacing and 0.15 m height. D: On top of the hammer B2 deposits at Verdolino showing widely-spaced ripple-like structures (circled). Structure spacing is about 0.5 m and height about 0.05 m. E: The coin points to the fine-ash layer at Camaldoli.

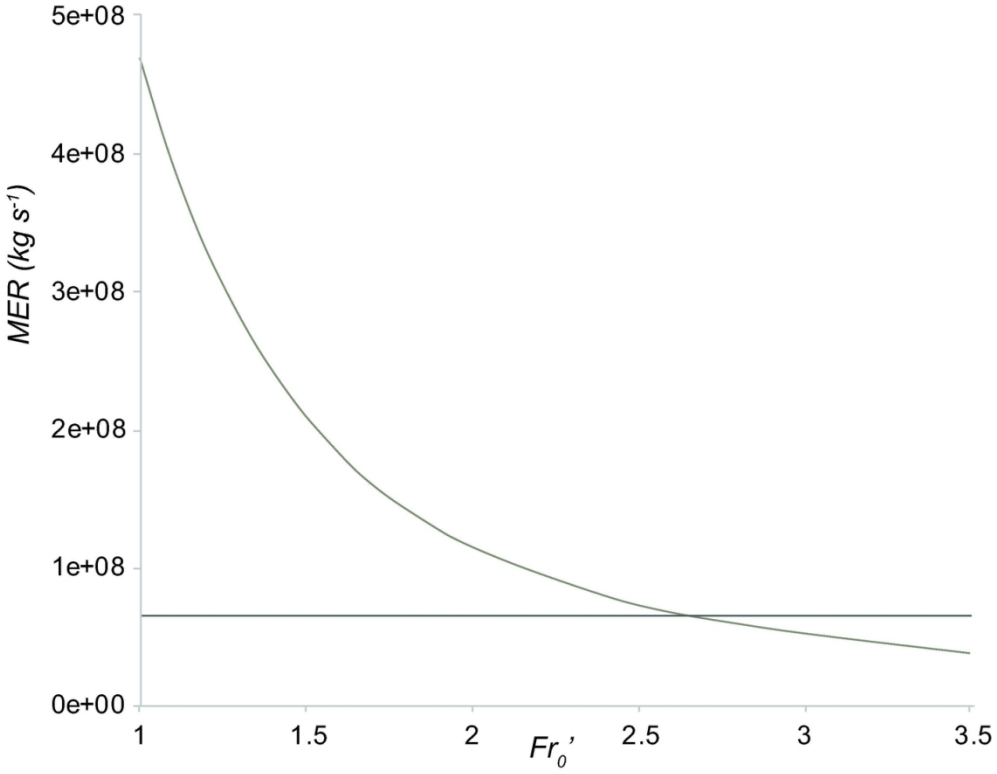

Diagram showing the relationship between Mass Eruption Rate (MER) and Desimetric Froude number (Fr0') for the B2 phase of the Agnano Monte-Spina eruption, as obtained by model application. The line intersecting the curve represents the value of MER calculated by the deposit volume data of Dell'Erba (2004).

120x94mm (300 x 300 DPI)

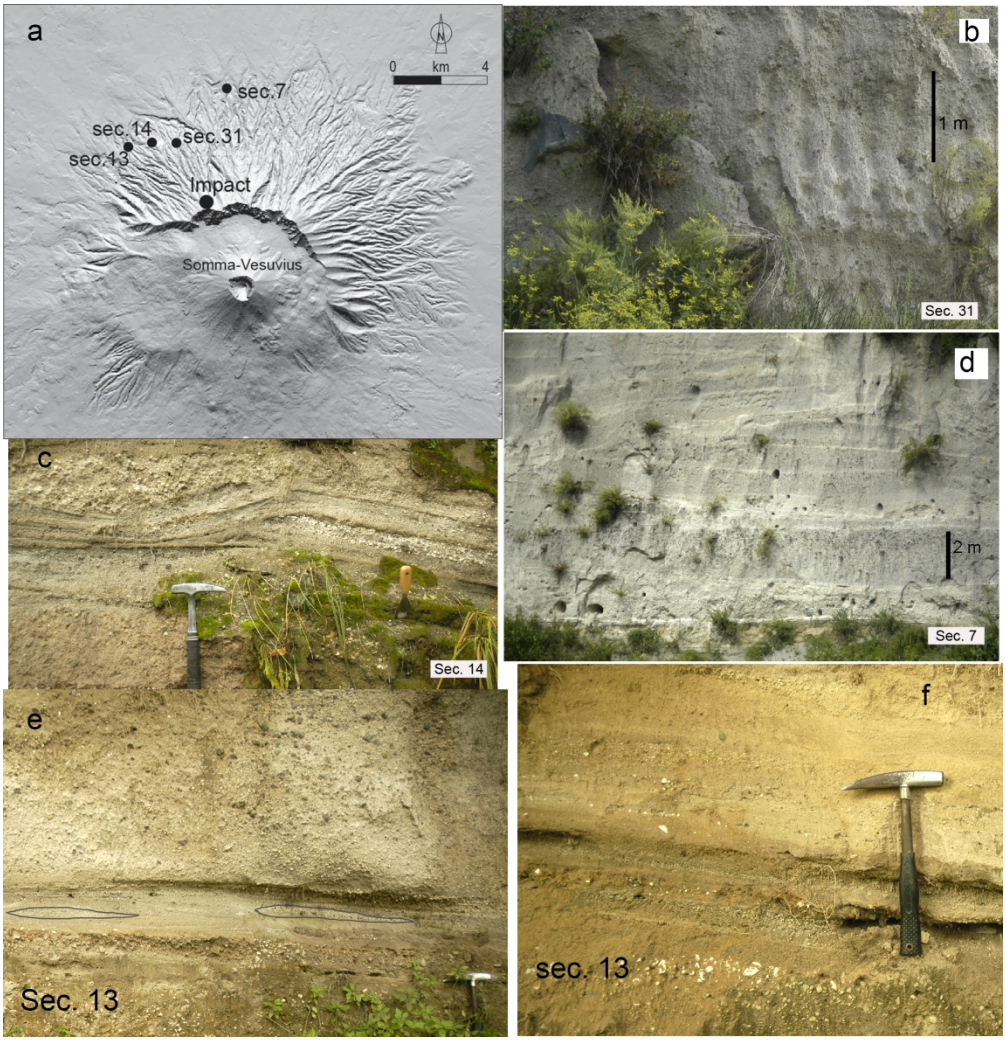

Display mount showing the Mercato eruption deposits used as a case study. The hammer used as a scale for field photographs, is 30 cm long. A: Digital Elevation Model map of Vesuvius. The location of deposits are marked, together with the zone of impact of the eruptive fountain. B: the massive layer formed at the impact of the eruptive fountain. C: the stratified layer formed at the bedload of the suspension current. D: the massive deposit emplaced by freezing at the break-in slope. E: the stratified layer at the base of the massive layer at the split location. Small dune structures are circled. Structure spacing is about 1 m, height about 0.1 m. F: the stratified layer on top of the massive layer at the split location

Nr	S_r ($kgm^{-2}s^{-1}$)	Q_b (m^2s^{-1})	S_{rw} (m^2s^{-1})	S_{rw}/Q_b	u_{avg} (ms^{-1})	u_* (ms^{-1})	D_{sm} (mm)	C_1 (-)	C_2 (-)	Qb^* (m^2s^{-1})	*structure*	*Origin*
1	1.10E+02	4.70E-04	1.00E-01	2.13E+02	-	0.26	0.75	5.95E-02	4.54E-03	3.55E-03	LAMass	Exp
2	2.20E+02	1.52E-03	2.00E-01	1.32E+02	-	0.44	0.65	3.19E-02	2.60E-03	4.92E-03	LAMass	Exp
3	1.38E+02	9.27E-05	1.25E-01	1.35E+03	-	0.14	0.53	6.28E-02	8.83E-04	4.67E-04	LAMass	Exp
4	3.90E+01	1.90E-04	3.00E-02	1.58E+02	-	0.26	0.57	3.35E-02	2.00E-03	3.61E-03	LAMass	Exp
5	1.60E+02	2.00E-03	2.00E-01	1.00E+02	-	0.4	0.08	1.89E-02	7.00E-04	6.96E-04	FAMass	Exp
6	7.80E-01	6.07E-05	3.50E-04	5.77E+00	5.52	0.36	0.64	-	3.54E-03	-	CARip.narr	Exp
7	1.17E+00	1.07E-03	9.75E-03	9.11E+00	9.74	0.66	0.63	-	4.60E-03	-	CARip.wide	Exp
8	6.80E-01	1.02E-04	2.60E-04	2.55E+00	8.83	0.55	0.64	-	1.30E-03	-	CARip.wide	Exp
9	1.90E-01	2.36E-06	8.20E-05	3.47E+01	4.77	0.30	0.64	-	7.83E-04	-	CARip.narr	Exp
10	6.10E-01	7.40E-06	2.80E-04	3.78E+01	3.05	0.27	0.77	-	2.41E-03	-	CARip.narr	Exp
11	1.90E-02	1.54E-05	1.50E-05	9.74E-01	4.8	0.27	0.073	-	5.950E-04	-	MARip.wide	Exp
12	4.20E-01	1.15E-03	2.80E-04	2.43E-01	13	0.73	0.79	-	3.50E-03		CARip.wide	Exp
13	2.20E-02	1.77E-07	1.78E-05	1.01E+02	3.56	0.17	0.044	-	5.950E-04	-	FAStrless	Exp
14	1.91E+03	1.53E-02	1.53E-00	1.00E+02	-	1.18	0.9	-	9.00E-03		LAMass	Nat (Sbirri)
15	5.09E-01	2.20E-02	4.70E-04	2.14E-02	63,29	2.72	0.8	-	1.00 E-03		LASmDune	Nat (Sbirri)
16	1.90E-01	2.90 E-03	1.53E-04	5.28E-02	31.3	1.43	0.24	-	1.00 E-03		CARip.wide	Nat (Verdolino)
17	8.20E-02	6.66E-07	6.66E-05	1.00E+02	9.50	0.43	0.073	-	6.00E-04		FAStrless	Nat (Camaldoli)
18	5.89E-01	1.10E-02	4.00E-04	3.64E-02	30	2.00	0.5	-	1.75 E-03		LASmDune	Nat (Mercato)

Table 2. Parameters used for the calculation of sedimentation and bedload transportation rates. For symbols see symbol list.

Eruption	*Location*	H_{tot} *(m)*	u_* *(m/s)*	τ *(Pa)*	ρ_f *(kgm^{-3})*	C_2 *(-)*
Agnano-Monte Spina	Sbirri	1685	2.72	18.63	2.52	0.0010
	Verdolino	290	1.43	6.02	2.94	0.0010
Mercato	Sandwich location	380	1.40	14.92	3.54	0.0013

Parameters of the dilute currents used as input for the calculation of sedimentation and transportation rates for the deposits of Campi Flegrei and Vesuvius eruptions used as case studies.

Table 2. Results of model calculations: flow field variables of PDCs. For symbol description see Table A.1.

Symbol	description	dimension
A_r	Rate of deposit aggradation	ms^{-1}
C_0	Reference known concentration (0.75)	-
C_d	Particle drag coefficient	-
C_i	Particle volumetric concentration of the i_{th} size	-
C_{tot}	Total particle volumetric concentration	-
C_1	Particle volumetric concentration in the fountain	-
C_2	Particle volumetric concentration in the dilute current	-
D	particle size	mm
D_i	diameter of the i_{th} size fraction	mm
D_{sm}	diameter of the median size	mm
d	Layer thickness	mm
Fr'_0	Densimetric Froude number	-
g	Gravity acceleration (9.81)	ms^{-2}
g'	Reduced gravity	ms^{-2}
H_{dep}	Deposit thickness	m
H_{tot}	Total flow thickness	m
k	Von Karman constant (0.4)	-
k_s	Ground roughness	m
MER	Mass Eruption rate	kgs^{-1}
P_n	Particle Rouse number	-
P_n*	Normalized Rouse number	-
P_{navg}	Average Rouse number of the particle load	-
P_{ni}	Rouse number of the ith particle-size class	-
P_{nsusp}	Rouse number at maximum suspension capacity	-
Q_b	Bedload transportation rate per unit width	m^2s^{-1}
Q_b^*	Bedload transportation rate per unit width normalized to one mm	m^2s^{-1}
Q_s	Area specific mass flow rate	$Kgm^{-2}s^{-1}$
r	Vent diameter	m
Re_*	Reynolds' number	-
S_r	Sedimentation rate	$kgm^{-2}s^{-1}$
S_{ri}	Sedimentation rate of the ith particle-size fraction	$kgm^{-2}s^{-1}$
S_{rw}	Sedimentation rate per unit width	m^2s^{-1}
t	Aggradation time	s
u_*	Flow shear velocity	ms^{-1}
u_{avg}	Height averaged flow velocity	ms^{-1}
U_f	Impact speed of the fountain	ms^{-1}
V_0	Exit velocity at the vent	ms^{-1}
w_t	Particle terminal velocity	ms^{-1}
w_{ti}	Terminal velocity of the ith particle-size class	ms^{-1}
y	Flow vertical coordinate	m
y_0	Specific height of C_0	-
ϕ	Unit of grain-size distribution ($\phi = -log_2 d$)	-
ϕ_i	Weight fraction of the i_{th} size class	Weight%
γ	Proportion of particles settling from suspension	-
γ_i	Proportion of particles settling from suspension of the ith size class	-

θ	Shields' number	-
θ_t	Critical Shield's number	-
$\theta_{tmedian}$	Shield's number of the median size	-
μ	viscosity	Pas
ρ_{atm}	Atmosphere density	kgm^{-3}
ρ_{dep}	Deposit density ($0.6\rho_s$)	kgm^{-3}
ρ_{mix}	Density of the gas-particle mixture	kgm^{-3}
ρ_g	Gas density	kgm^{-3}
ρ_s	Particle density	kgm^{-3}
ρ_{si}	Density of the ith particle-size class	kgm^{-3}
τ	Shear stress at the base of the current	Pa
τ_{ri}	minimum shear of the i_{th} size fraction	Pa
τ_{rsm}	minimum shear stress of the particle mixture	Pa
τ_{rsm}^*	Shield number normalized to the mixture	-

List of symbols, with description and physical dimension

u_* (ms^{-1})	0.137
ρ_s average (kgm^{-3})	1815
C_{tot} (-)	0.0628
ρ_{mix} (kgm^{-3})	125.6
τ (Pa)	2.357
D_{sm} (mm)	0.53
Re_* (-)	459
θ_t (-)	0.015
τ_{rsm}^* (-)	0.0112
τ_{rsm} (Pa)	0.1313
S_r ($kgm^{-2}s^{-1}$)	138
ρ_{dep} (kgm^{-3})	1100
A_r (ms^{-1})	0.125

Component	D_i (m)	D_i/D_{sm}	τ_{ri} (Pa)	τ/τ_{ri}	W_i^*	Q_{bi} (m^2s^{-1})	ϕ_i	ρ_{si} (kgm^{-3})
dense lithic	5.66E-03	9.725	0.603	4.188	1.057	1.814E-07	0.0083	2588
dense lithic	4.00E-03	6.873	0.475	5.314	1.539	3.709E-07	0.0116	2588
dense lithic	2.83E-03	4.863	0.366	6.902	2.154	1.104E-06	0.0247	2588
dense lithic	2.00E-03	3.436	0.271	9.329	2.947	1.742E-06	0.0285	2588
dense lithic	1.41E-03	2.423	0.201	12.574	3.788	2.265E-06	0.0288	2588
dense lithic	1.00E-03	1.718	0.161	15.719	4.434	5.425E-06	0.0590	2588
dense lithic	7.07E-04	1.215	0.139	18.173	4.855	5.313E-06	0.0527	2588
dense lithic	5.00E-04	0.859	0.127	19.906	5.118	4.713E-06	0.0444	2588
dense lithic	3.54E-04	0.608	0.119	21.174	5.296	5.115E-06	0.0465	2588
dense lithic	2.50E-04	0.430	0.114	22.208	5.433	4.102E-06	0.0364	2588
dense lithic	1.77E-04	0.304	0.109	23.129	5.549	3.397E-06	0.0295	2588
dense lithic	1.25E-04	0.215	0.105	24.027	5.657	3.189E-06	0.0272	2588
dense lithic	8.84E-05	0.152	0.101	24.934	5.762	3.549E-06	0.0297	2588
dense lithic	6.25E-05	0.107	0.098	25.878	5.867	2.845E-06	0.0234	2588
dense lithic	4.42E-05	0.076	0.094	26.870	5.973	2.946E-06	0.0238	2588
dense lithic	3.13E-05	0.054	0.090	27.914	6.079	2.304E-06	0.0183	2588
dense lithic	2.21E-05	0.038	0.087	29.028	6.188	2.535E-06	0.0197	2588
dense lithic	1.56E-05	0.027	0.084	30.206	6.298	1.843E-06	0.0141	2588
dense lithic	1.10E-05	0.019	0.080	31.453	6.409	7.305E-07	0.0055	2588
vesicular glass	5.66E-03	9.725	0.603	4.188	1.057	3.242E-07	0.0148	686
vesicular glass	4.00E-03	6.873	0.475	5.314	1.539	1.180E-06	0.0369	733
vesicular glass	2.83E-03	4.863	0.366	6.902	2.154	1.477E-06	0.0330	783
vesicular glass	2.00E-03	3.436	0.271	9.329	2.947	3.134E-06	0.0512	837
vesicular glass	1.41E-03	2.423	0.201	12.574	3.788	4.127E-06	0.0525	894
vesicular glass	1.00E-03	1.718	0.161	15.719	4.434	2.105E-06	0.0229	956
vesicular glass	7.07E-04	1.215	0.139	18.173	4.855	1.812E-06	0.0180	1021
vesicular glass	5.00E-04	0.859	0.127	19.906	5.118	2.597E-06	0.0244	1091

vesicular glass	3.54E-04	0.608	0.119	21.174	5.296	1.580E-06	0.0144	1166
vesicular glass	2.50E-04	0.430	0.114	22.208	5.433	1.979E-06	0.0175	1245
vesicular glass	1.77E-04	0.304	0.109	23.129	5.549	1.273E-06	0.0111	1331
vesicular glass	1.25E-04	0.215	0.105	24.027	5.657	1.194E-06	0.0102	1422
vesicular glass	8.84E-05	0.152	0.101	24.934	5.762	1.329E-06	0.0111	1519
vesicular glass	6.25E-05	0.107	0.098	25.878	5.867	1.066E-06	0.0087	1623
vesicular glass	4.42E-05	0.076	0.094	26.870	5.973	1.103E-06	0.0089	1734
vesicular glass	3.13E-05	0.054	0.090	27.914	6.079	8.629E-07	0.0068	1853
vesicular glass	2.21E-05	0.038	0.087	29.028	6.188	9.494E-07	0.0074	1979
vesicular glass	1.56E-05	0.027	0.084	30.206	6.298	6.902E-07	0.0053	2115
vesicular glass	1.10E-05	0.019	0.080	31.453	6.409	2.736E-07	0.0021	2259
salic xx	1.00E-03	1.718	0.161	15.719	4.434	8.907E-08	0.0010	2400
salic xx	7.07E-04	1.215	0.139	18.173	4.855	2.483E-07	0.0025	2400
salic xx	5.00E-04	0.859	0.127	19.906	5.118	4.730E-07	0.0045	2400
salic xx	3.54E-04	0.608	0.119	21.174	5.296	6.500E-07	0.0059	2400
salic xx	2.50E-04	0.430	0.114	22.208	5.433	5.596E-07	0.0050	2400
salic xx	1.77E-04	0.304	0.109	23.129	5.549	4.702E-07	0.0041	2400
salic xx	1.25E-04	0.215	0.105	24.027	5.657	3.286E-07	0.0028	2400
salic xx	8.84E-05	0.152	0.101	24.934	5.762	3.658E-07	0.0031	2400
salic xx	6.25E-05	0.107	0.098	25.878	5.867	2.932E-07	0.0024	2400
salic xx	4.42E-05	0.076	0.094	26.870	5.973	3.036E-07	0.0024	2400
salic xx	3.13E-05	0.054	0.090	27.914	6.079	2.375E-07	0.0019	2400
salic xx	2.21E-05	0.038	0.087	29.028	6.188	2.613E-07	0.0020	2400
salic xx	1.56E-05	0.027	0.084	30.206	6.298	1.899E-07	0.0015	2400
salic xx	1.10E-05	0.019	0.080	31.453	6.409	7.528E-08	0.0006	2400
femic xx	1.00E-03	1.718	0.161	15.719	4.434	1.700E-07	0.0018	3280
femic xx	7.07E-04	1.215	0.139	18.173	4.855	6.615E-07	0.0066	3280
femic xx	5.00E-04	0.859	0.127	19.906	5.118	8.095E-07	0.0076	3280
femic xx	3.54E-04	0.608	0.119	21.174	5.296	1.228E-06	0.0112	3280
femic xx	2.50E-04	0.430	0.114	22.208	5.433	1.139E-06	0.0101	3280

femic xx	1.77E-04	0.304	0.109	23.129	5.549	7.783E-07	0.0068	3280
femic xx	1.25E-04	0.215	0.105	24.027	5.657	5.393E-07	0.0046	3280
femic xx	8.84E-05	0.152	0.101	24.934	5.762	6.005E-07	0.0050	3280
femic xx	6.25E-05	0.107	0.098	25.878	5.867	4.814E-07	0.0040	3280
femic xx	4.42E-05	0.076	0.094	26.870	5.973	4.985E-07	0.0040	3280
femic xx	3.13E-05	0.054	0.090	27.914	6.079	3.898E-07	0.0031	3280
femic xx	2.21E-05	0.038	0.087	29.028	6.188	4.289E-07	0.0033	3280
femic xx	1.56E-05	0.027	0.084	30.206	6.298	3.118E-07	0.0024	3280
femic xx	1.10E-05	0.019	0.080	31.453	6.409	1.236E-07	0.0009	3280
							1	
					Q_b (m^2s^{-1})	9.543E-05		

Supporting file A. Step-by-step calculation of the bedload transportation rate Q_b of an experimental massive deposit formed at the column impact. In yellow the main parametres. For symbols see the symbol list.

u_* (ms^{-1})	0.66
ρ_s average (kgm^{-3})	2367
C_{tot} (-)	0.0046
ρ_{mix} (kgm^{-3})	12.11
τ (Pa)	5.274
D_{sm} (mm)	0.629
Re_* (-)	256
θ_t (-)	0.01
τ_{rsm}^* (-)	0.0075
τ_{rsm} (Pa)	0.1090
S_r (kgm^{-2}s^{-1})	1.17
ρ_{dep} (kgm^{-3})	1200
A_r (ms^{-1})	0.000975

Component	D_i (m)	D_i/D_{sm}	τ_{ri} (Pa)	τ/τ_{ri}	W_i^*	Q_{bi} (m^{2}s^{-1})	ϕ_i	ρ_{si} (kgm^{-3})
dense lithic	5.66E-03	8.998	0.475	11.114	3.436	8.332E-06	0.0161	2588
dense lithic	4.00E-03	6.359	0.373	14.147	4.128	2.082E-05	0.0335	2588
dense lithic	2.83E-03	4.499	0.285	18.535	4.912	3.706E-05	0.0501	2588
dense lithic	2.00E-03	3.180	0.209	25.183	5.790	5.872E-05	0.0673	2588
dense lithic	1.41E-03	2.242	0.157	33.552	6.584	7.089E-05	0.0715	2588
dense lithic	1.00E-03	1.590	0.128	41.147	7.125	8.101E-05	0.0754	2588
dense lithic	7.07E-04	1.124	0.113	46.878	7.459	7.881E-05	0.0701	2588
dense lithic	5.00E-04	0.795	0.104	50.921	7.665	7.359E-05	0.0637	2588
dense lithic	3.54E-04	0.563	0.098	53.938	7.807	6.150E-05	0.0523	2588
dense lithic	2.50E-04	0.397	0.093	56.459	7.917	4.996E-05	0.0419	2588
dense lithic	1.77E-04	0.281	0.090	58.750	8.012	3.261E-05	0.0270	2588
dense lithic	1.25E-04	0.199	0.086	61.011	8.102	2.791E-05	0.0229	2588
dense lithic	8.84E-05	0.141	0.083	63.311	8.188	3.609E-05	0.0293	2588
dense lithic	6.25E-05	0.099	0.080	65.713	8.275	2.300E-05	0.0184	2588
dense lithic	4.42E-05	0.070	0.077	68.241	8.362	2.124E-05	0.0169	2588
dense lithic	3.13E-05	0.050	0.074	70.904	8.448	1.628E-05	0.0128	2588
dense lithic	2.21E-05	0.035	0.072	73.744	8.537	1.531E-05	0.0119	2588
dense lithic	1.56E-05	0.025	0.069	76.747	8.625	9.563E-06	0.0074	2588
dense lithic	1.10E-05	0.017	0.066	79.925	8.714	3.203E-06	0.0024	2588
vesicular glass	5.66E-03	8.998	0.475	11.114	3.436	1.088E-06	0.0021	686
vesicular glass	4.00E-03	6.359	0.373	14.147	4.128	4.336E-06	0.0070	733
vesicular glass	2.83E-03	4.499	0.285	18.535	4.912	8.042E-06	0.0109	783
vesicular glass	2.00E-03	3.180	0.209	25.183	5.790	1.395E-05	0.0160	837
vesicular glass	1.41E-03	2.242	0.157	33.552	6.584	1.607E-05	0.0162	894
vesicular glass	1.00E-03	1.590	0.128	41.147	7.125	1.200E-05	0.0112	956
vesicular glass	7.07E-04	1.124	0.113	46.878	7.459	1.048E-05	0.0093	1021
vesicular glass	5.00E-04	0.795	0.104	50.921	7.665	1.575E-05	0.0136	1091

vesicular glass	3.54E-04	0.563	0.098	53.938	7.807	1.230E-05	0.0105	1166
vesicular glass	2.50E-04	0.397	0.093	56.459	7.917	1.339E-05	0.0112	1245
vesicular glass	1.77E-04	0.281	0.090	58.750	8.012	1.801E-05	0.0149	1331
vesicular glass	1.25E-04	0.199	0.086	61.011	8.102	1.708E-05	0.0140	1422
vesicular glass	8.84E-05	0.141	0.083	63.311	8.188	2.209E-05	0.0179	1519
vesicular glass	6.25E-05	0.099	0.080	65.713	8.275	1.408E-05	0.0113	1623
vesicular glass	4.42E-05	0.070	0.077	68.241	8.362	1.300E-05	0.0103	1734
vesicular glass	3.13E-05	0.050	0.074	70.904	8.448	9.968E-06	0.0078	1853
vesicular glass	2.21E-05	0.035	0.072	73.744	8.537	9.369E-06	0.0073	1979
vesicular glass	1.56E-05	0.025	0.069	76.747	8.625	5.853E-06	0.0045	2115
vesicular glass	1.10E-05	0.017	0.066	79.925	8.714	1.961E-06	0.0015	2259
salic xx	1.41E-03	2.242	0.157	33.552	6.584	6.102E-07	0.0006	2400
salic xx	7.07E-04	1.124	0.113	46.878	7.459	3.514E-06	0.0031	2400
salic xx	5.00E-04	0.795	0.104	50.921	7.665	5.269E-06	0.0046	2400
salic xx	3.54E-04	0.563	0.098	53.938	7.807	6.150E-06	0.0052	2400
salic xx	2.50E-04	0.397	0.093	56.459	7.917	6.604E-06	0.0055	2400
salic xx	1.77E-04	0.281	0.090	58.750	8.012	4.208E-06	0.0035	2400
salic xx	1.25E-04	0.199	0.086	61.011	8.102	4.130E-06	0.0034	2400
salic xx	8.84E-05	0.141	0.083	63.311	8.188	5.341E-06	0.0043	2400
salic xx	6.25E-05	0.099	0.080	65.713	8.275	3.403E-06	0.0027	2400
salic xx	4.42E-05	0.070	0.077	68.241	8.362	3.143E-06	0.0025	2400
salic xx	3.13E-05	0.050	0.074	70.904	8.448	2.410E-06	0.0019	2400
salic xx	2.21E-05	0.035	0.072	73.744	8.537	2.265E-06	0.0018	2400
salic xx	1.56E-05	0.025	0.069	76.747	8.625	1.415E-06	0.0011	2400
salic xx	1.10E-05	0.017	0.066	79.925	8.714	4.740E-07	0.0004	2400
femic xx	1.00E-03	1.590	0.128	41.147	7.125	3.027E-06	0.0028	3280
femic xx	7.07E-04	1.124	0.113	46.878	7.459	8.757E-06	0.0078	3280
femic xx	5.00E-04	0.795	0.104	50.921	7.665	5.269E-06	0.0046	3280
femic xx	3.54E-04	0.563	0.098	53.938	7.807	1.351E-05	0.0115	3280
femic xx	2.50E-04	0.397	0.093	56.459	7.917	1.082E-05	0.0091	3280

femic xx	1.77E-04	0.281	0.090	58.750	8.012	7.178E-06	0.0059	3280
femic xx	1.25E-04	0.199	0.086	61.011	8.102	6.758E-06	0.0055	3280
femic xx	8.84E-05	0.141	0.083	63.311	8.188	8.740E-06	0.0071	3280
femic xx	6.25E-05	0.099	0.080	65.713	8.275	5.569E-06	0.0045	3280
femic xx	4.42E-05	0.070	0.077	68.241	8.362	5.143E-06	0.0041	3280
femic xx	3.13E-05	0.050	0.074	70.904	8.448	3.943E-06	0.0031	3280
femic xx	2.21E-05	0.035	0.072	73.744	8.537	3.707E-06	0.0029	3280
femic xx	1.56E-05	0.025	0.069	76.747	8.625	2.316E-06	0.0018	3280
femic xx	1.10E-05	0.017	0.066	79.925	8.714	7.756E-07	0.0006	3280
					Q_b (m^2s^{-1})	1.079E-03	1	

Supporting file B. Step-by-step calculation of the bedload transportation rate Q_b of an experimental layer with ripple-like structures sedimented by the dilute turbulent suspension current formed as a lateral evolution of the column impact. In yellow the main parametres. For symbols see the symbol list.

u_* (ms^{-1})	0.17
ρ_s average (kgm^{-3})	2241
C_{tot} (-)	0.00060
ρ_{mix} (kgm^{-3})	2.55
τ (Pa)	0.074
D_{sm} (mm)	0.044
Re_* (-)	0.90
θ_t (-)	0.019
$\tau_{rsm}{}^*$ (-)	0.0143
τ_{rsm} (Pa)	0.0250
S_r (kgm^{-2}s^{-1})	0.024
ρ_{dep} (kgm^{-3})	1344.6
A_r (ms^{-1})	1.78E-05

Component	D_i (m)	D_i/D_{sm}	τ_{ri} (Pa)	τ/τ_{ri}	W_i^*	Q_{bi} (m^{2}s^{-1})	ϕ_i
vesicular glass	2.00E-03	45.455	0.323	0.229	2.607E-06	4.307E-14	0.0289
vesicular glass	1.41E-03	32.045	0.255	0.289	7.480E-06	6.504E-14	0.0152
vesicular glass	1.00E-03	22.727	0.203	0.364	2.108E-05	2.016E-13	0.0167
vesicular glass	7.07E-04	16.068	0.161	0.459	5.995E-05	6.255E-13	0.0183
vesicular glass	5.00E-04	11.364	0.128	0.579	1.704E-04	2.371E-12	0.0244
vesicular glass	3.54E-04	8.045	0.101	0.731	4.869E-04	8.044E-12	0.0289
vesicular glass	2.50E-04	5.682	0.079	0.937	1.490E-03	4.016E-11	0.0472
vesicular glass	1.77E-04	4.023	0.059	1.243	5.327E-03	1.714E-10	0.0563
vesicular glass	1.25E-04	2.841	0.044	1.693	7.510E-02	3.527E-09	0.0822
vesicular glass	8.84E-05	2.009	0.034	2.201	2.203E-01	1.321E-08	0.1050
vesicular glass	6.25E-05	1.420	0.028	2.633	3.815E-01	3.062E-08	0.1405
vesicular glass	4.42E-05	1.005	0.025	2.944	5.101E-01	5.087E-08	0.1746
vesicular glass	3.13E-05	0.711	0.023	3.166	6.051E-01	4.503E-08	0.1303
vesicular glass	2.21E-05	0.502	0.022	3.338	6.804E-01	3.340E-08	0.0859
vesicular glass	1.56E-05	0.355	0.021	3.486	7.456E-01	1.540E-08	0.0361
vesicular glass	1.10E-05	0.250	0.020	3.625	8.073E-01	4.372E-09	0.0095
					Q_b (m^{2}s^{-1})	1.77E-07	1

Supporting file C. Step-by-step calculation of the bedload transportation rate Q_b of an experimental fine-ash structureless thin layer formed by a dilute suspension current fed with the fine material. In yellow the main parametres. For symbols see the symbol list.

u_* (ms^{-1})	1.176
ρ_s average (kgm^{-3})	1757
C_{tot} (-)	0.009
ρ_{mix} (kgm^{-3})	16.19
τ (Pa)	22.41
D_{sm} (mm)	0.9
Re_* (-)	856
θ_t (-)	0.01
τ_{rsm}^* (-)	0.0075
τ_{rsm} (Pa)	0.081

Component	D_i (m)	D_i/D_{sm}	τ_{ri} (Pa)	τ/τ_{ri}	W_i^*	Q_{bi} (m^{2}s^{-1})	ϕ_i	ρ_{si} (kgm^{-3})
vesicular glass	3.20E-02	35.556	0.882	25.422	5.817	1.789E-04	0.0199	474
vesicular glass	2.24E-02	24.889	0.694	32.284	6.480	3.167E-04	0.0317	474
vesicular glass	1.60E-02	17.778	0.554	40.448	7.081	2.704E-04	0.0247	474
vesicular glass	1.13E-02	12.556	0.439	51.063	7.672	3.420E-04	0.0289	474
vesicular glass	8.00E-03	8.889	0.348	64.414	8.229	4.169E-04	0.0328	531
vesicular glass	5.66E-03	6.289	0.273	81.975	8.769	5.732E-04	0.0423	596
vesicular glass	4.00E-03	4.444	0.208	107.641	9.333	5.048E-04	0.0350	669
vesicular glass	2.83E-03	3.144	0.153	146.189	9.908	4.438E-04	0.0290	751
vesicular glass	2.00E-03	2.222	0.115	194.053	10.387	6.202E-04	0.0387	842
vesicular glass	1.41E-03	1.567	0.094	238.133	10.703	6.324E-04	0.0383	945
vesicular glass	1.00E-03	1.111	0.083	270.351	10.886	4.042E-04	0.0240	1060
vesicular glass	7.07E-04	0.786	0.076	293.354	10.999	4.126E-04	0.0243	1189
vesicular glass	5.00E-04	0.556	0.072	310.601	11.076	4.050E-04	0.0237	1334
vesicular glass	3.54E-04	0.393	0.069	324.923	11.136	4.209E-04	0.0245	1497
vesicular glass	2.50E-04	0.278	0.066	338.161	11.187	4.117E-04	0.0238	1679
vesicular glass	1.77E-04	0.197	0.064	351.067	11.235	3.923E-04	0.0226	1884
vesicular glass	1.25E-04	0.139	0.062	364.357	11.282	3.651E-04	0.0210	2114
vesicular glass	8.84E-05	0.098	0.059	378.174	11.328	2.129E-04	0.0122	2372
vesicular glass	6.25E-05	0.069	0.057	392.744	11.374	2.388E-04	0.0136	2560
vesicular glass	4.42E-05	0.049	0.055	408.138	11.420	2.888E-04	0.0164	2560
vesicular glass	3.13E-05	0.035	0.053	424.353	11.466	2.781E-04	0.0157	2560
vesicular glass	2.21E-05	0.025	0.051	441.629	11.512	3.698E-04	0.0208	2560
vesicular glass	1.56E-05	0.017	0.049	459.868	11.559	3.405E-04	0.0191	2560
vesicular glass	1.10E-05	0.012	0.047	479.133	11.605	3.025E-04	0.0169	2560
vesicular glass	8.00E-06	0.009	0.045	497.556	11.646	2.061E-04	0.0115	2560
vesicular glass	5.60E-06	0.006	0.043	519.185	11.692	1.345E-04	0.0074	2560
vesicular glass	4.00E-06	0.004	0.041	540.573	11.735	7.021E-05	0.0039	2560
vesicular glass	2.80E-06	0.003	0.040	564.315	11.780	3.957E-05	0.0022	2560

vesicular glass	2.00E-06	0.002	0.038	587.748	11.822	2.084E-05	0.0011	2560
salic xx	2.00E-03	2.222	0.115	194.053	10.387	1.227E-05	0.0008	2400
salic xx	1.41E-03	1.567	0.094	238.133	10.703	3.314E-05	0.0020	2400
salic xx	1.00E-03	1.111	0.083	270.351	10.886	1.110E-04	0.0066	2400
salic xx	7.07E-04	0.786	0.076	293.354	10.999	1.923E-04	0.0113	2400
salic xx	5.00E-04	0.556	0.072	310.601	11.076	3.004E-04	0.0176	2400
salic xx	3.54E-04	0.393	0.069	324.923	11.136	2.343E-04	0.0136	2400
salic xx	2.50E-04	0.278	0.066	338.161	11.187	2.488E-04	0.0144	2400
salic xx	1.77E-04	0.197	0.064	351.067	11.235	1.541E-04	0.0089	2400
salic xx	1.25E-04	0.139	0.062	364.357	11.282	1.041E-04	0.0060	2400
salic xx	8.84E-05	0.098	0.059	378.174	11.328	5.787E-05	0.0033	2400
salic xx	6.25E-05	0.069	0.057	392.744	11.374	5.709E-05	0.0033	2400
salic xx	4.42E-05	0.049	0.055	408.138	11.420	6.158E-05	0.0035	2400
salic xx	3.13E-05	0.035	0.053	424.353	11.466	5.352E-05	0.0030	2400
salic xx	2.21E-05	0.025	0.051	441.629	11.512	6.484E-05	0.0036	2400
salic xx	1.56E-05	0.017	0.049	459.868	11.559	5.482E-05	0.0031	2400
salic xx	1.10E-05	0.012	0.047	479.133	11.605	4.501E-05	0.0025	2400
salic xx	8.00E-06	0.009	0.045	497.556	11.646	2.851E-05	0.0016	2400
salic xx	5.60E-06	0.006	0.043	519.185	11.692	1.737E-05	0.0010	2400
salic xx	4.00E-06	0.004	0.041	540.573	11.735	8.511E-06	0.0005	2400
salic xx	2.80E-06	0.003	0.040	564.315	11.780	4.518E-06	0.0002	2400
salic xx	2.00E-06	0.002	0.038	587.748	11.822	2.247E-06	0.0001	2400
dense lithic	3.20E-02	35.556	0.882	25.422	5.817	1.106E-06	0.0001	2570
dense lithic	2.24E-02	24.889	0.694	32.284	6.480	1.232E-06	0.0001	2570
dense lithic	1.60E-02	17.778	0.554	40.448	7.081	1.346E-06	0.0001	2570
dense lithic	1.13E-02	12.556	0.439	51.063	7.672	2.166E-05	0.0018	2570
dense lithic	8.00E-03	8.889	0.348	64.414	8.229	6.296E-05	0.0050	2570
dense lithic	5.66E-03	6.289	0.273	81.975	8.769	2.280E-04	0.0168	2570
dense lithic	4.00E-03	4.444	0.208	107.641	9.333	2.128E-04	0.0148	2570
dense lithic	2.83E-03	3.144	0.153	146.189	9.908	3.335E-04	0.0218	2570

dense lithic	2.00E-03	2.222	0.115	194.053	10.387	3.428E-04	0.0214	2570
dense lithic	1.41E-03	1.567	0.094	238.133	10.703	2.996E-04	0.0181	2570
dense lithic	1.00E-03	1.111	0.083	270.351	10.886	4.593E-04	0.0273	2570
dense lithic	7.07E-04	0.786	0.076	293.354	10.999	4.294E-04	0.0253	2570
dense lithic	5.00E-04	0.556	0.072	310.601	11.076	3.600E-04	0.0211	2570
dense lithic	3.54E-04	0.393	0.069	324.923	11.136	3.813E-04	0.0222	2570
dense lithic	2.50E-04	0.278	0.066	338.161	11.187	2.835E-04	0.0164	2570
dense lithic	1.77E-04	0.197	0.064	351.067	11.235	1.897E-04	0.0109	2570
dense lithic	1.25E-04	0.139	0.062	364.357	11.282	1.493E-04	0.0086	2570
dense lithic	8.84E-05	0.098	0.059	378.174	11.328	7.863E-05	0.0045	2570
dense lithic	6.25E-05	0.069	0.057	392.744	11.374	7.812E-05	0.0044	2570
dense lithic	4.42E-05	0.049	0.055	408.138	11.420	8.479E-05	0.0048	2570
dense lithic	3.13E-05	0.035	0.053	424.353	11.466	7.408E-05	0.0042	2570
dense lithic	2.21E-05	0.025	0.051	441.629	11.512	9.017E-05	0.0051	2570
dense lithic	1.56E-05	0.017	0.049	459.868	11.559	7.655E-05	0.0043	2570
dense lithic	1.10E-05	0.012	0.047	479.133	11.605	6.309E-05	0.0035	2570
dense lithic	8.00E-06	0.009	0.045	497.556	11.646	4.009E-05	0.0022	2570
dense lithic	5.60E-06	0.006	0.043	519.185	11.692	2.451E-05	0.0014	2570
dense lithic	4.00E-06	0.004	0.041	540.573	11.735	1.204E-05	0.0007	2570
dense lithic	2.80E-06	0.003	0.040	564.315	11.780	6.405E-06	0.0004	2570
dense lithic	2.00E-06	0.002	0.038	587.748	11.822	3.194E-06	0.0002	2570

Q_b (m^2s^{-1})	0.0153
S_{rw} (m^2s^{-1})	1.53
A_r (ms^{-1})	1.53
U_f (ms^{-1})	170.60

Supporting file D. Step-by-step calculation of the bedload transportation rate $Q_{b,}$ sedimentation rate per unit width S_{rw}, aggradation rate A_r and collapse falling velocity U_f for the massive layer at Sbirri. In yellow the main parametres. For symbols see the symbol list.

Input data	
u^* (ms^{-1})	2.72
C_{tot}	0.00103
P_{nsusp}	0.6

Component	D_i (m)	P_{ni}	$P_{ni}{}^*C_{transi}$	$P_{ni}/P_n{}^*$	ρ_{si} (kgm^{-3})	w_t (ms^{-1})	ϕ_t	Vol. fraction (m^3kg^{-1})	C_{transi}	γ_i	γ_{truei}	S_{ri} ($kgm^{-2}s^{-1}$)	$\rho_{si}*\phi_t$ (kgm^{-3})
vesicular glass	1.60E-02	4.266	2.52E-04	1.31E+00	422	4.76	1.43E-02	3.39E-05	5.91E-05	4.42E-06	6.03E-06	1.21E-02	6.037
vesicular glass	1.13E-02	3.663	2.26E-04	1.13E+00	474	4.08	1.68E-02	3.55E-05	6.18E-05	5.38E-06	5.12E-06	9.91E-03	7.958
vesicular glass	8.00E-03	3.137	1.40E-04	9.65E-01	531	3.50	1.36E-02	2.56E-05	4.46E-05	4.52E-06	4.63E-06	8.60E-03	7.227
vesicular glass	5.66E-03	2.681	1.11E-04	8.25E-01	596	2.99	1.41E-02	2.36E-05	4.12E-05	4.87E-06	4.61E-06	8.22E-03	8.407
vesicular glass	4.00E-03	2.286	6.61E-05	7.03E-01	669	2.55	1.11E-02	1.66E-05	2.89E-05	4.00E-06	4.93E-06	8.41E-03	7.425
vesicular glass	2.83E-03	1.944	8.54E-05	5.98E-01	751	2.17	1.89E-02	2.52E-05	4.39E-05	7.11E-06	8.70E-06	1.42E-02	14.184
vesicular glass	2.00E-03	1.649	1.08E-04	5.07E-01	842	1.84	3.16E-02	3.75E-05	6.54E-05	1.24E-05	1.32E-05	2.04E-02	26.608
vesicular glass	1.41E-03	1.395	9.32E-05	4.29E-01	945	1.56	3.62E-02	3.83E-05	6.68E-05	1.49E-05	1.44E-05	2.11E-02	34.198
vesicular glass	1.00E-03	1.175	5.86E-05	3.62E-01	1060	1.31	3.03E-02	2.86E-05	4.98E-05	1.31E-05	1.38E-05	1.91E-02	32.115
vesicular glass	7.07E-04	0.984	4.83E-05	3.03E-01	1189	1.10	3.35E-02	2.82E-05	4.91E-05	1.53E-05	1.48E-05	1.93E-02	39.836
vesicular glass	5.00E-04	0.817	2.96E-05	2.51E-01	1334	0.91	2.77E-02	2.08E-05	3.62E-05	1.35E-05	1.39E-05	1.69E-02	36.956
vesicular glass	3.54E-04	0.670	2.22E-05	2.06E-01	1497	0.75	2.85E-02	1.90E-05	3.32E-05	1.49E-05	1.55E-05	1.73E-02	42.660
vesicular glass	2.50E-04	0.540	1.67E-05	1.66E-01	1679	0.60	2.97E-02	1.77E-05	3.08E-05	1.68E-05	1.57E-05	1.59E-02	49.878
vesicular glass	1.77E-04	0.425	8.23E-06	1.31E-01	1884	0.47	2.09E-02	1.11E-05	1.93E-05	1.31E-05	1.30E-05	1.16E-02	39.379
vesicular glass	1.25E-04	0.325	4.82E-06	1.00E-01	2114	0.36	1.80E-02	8.51E-06	1.48E-05	1.28E-05	1.20E-05	9.18E-03	38.051
vesicular glass	8.84E-05	0.238	2.17E-06	7.32E-02	2372	0.27	1.24E-02	5.23E-06	9.11E-06	1.02E-05	1.08E-05	6.78E-03	29.409
vesicular glass	6.25E-05	0.159	1.26E-06	4.89E-02	2560	0.18	1.16E-02	4.53E-06	7.90E-06	1.21E-05	1.40E-05	6.36E-03	29.696
vesicular glass	4.42E-05	0.090	7.24E-07	2.77E-02	2560	0.10	1.18E-02	4.61E-06	8.04E-06	1.84E-05	1.85E-05	4.75E-03	30.208
vesicular glass	3.13E-05	0.044	2.40E-07	1.35E-02	2560	0.05	8.04E-03	3.14E-06	5.48E-06	1.86E-05	1.89E-05	2.37E-03	20.582
vesicular glass	2.21E-05	0.018	7.61E-08	5.60E-03	2560	0.02	6.14E-03	2.40E-06	4.18E-06	1.95E-05	1.74E-05	9.05E-04	15.718

vesicular glass	1.56E-05	0.007	1.52E-08	2.09E-03	2560	0.01	3.29E-03	1.29E-06	2.24E-06	1.25E-05	1.00E-05	1.95E-04	8.422
vesicular glass	1.10E-05	0.002	1.63E-09	7.38E-04	2560	0.00	9.98E-04	3.90E-07	6.80E-07	4.11E-06	2.88E-06	1.99E-05	2.555
salic xx	2.83E-03	5.161	1.15E-06	1.59E+00	2400	5.76	3.08E-04	1.28E-07	2.24E-07	1.39E-08	1.91E-08	2.64E-04	0.739
salic xx	2.00E-03	4.176	1.72E-06	1.28E+00	2400	4.66	5.67E-04	2.36E-07	4.12E-07	3.15E-08	9.33E-08	1.04E-03	1.361
salic xx	1.41E-03	3.363	8.45E-06	1.03E+00	2400	3.75	3.46E-03	1.44E-06	2.51E-06	2.38E-07	6.22E-07	5.60E-03	8.304
salic xx	1.00E-03	2.683	3.45E-05	8.25E-01	2400	2.99	1.77E-02	7.38E-06	1.29E-05	1.52E-06	1.65E-06	1.18E-02	42.480
salic xx	7.07E-04	2.108	2.74E-05	6.48E-01	2400	2.35	1.79E-02	7.46E-06	1.30E-05	1.95E-06	2.60E-06	1.47E-02	42.960
salic xx	5.00E-04	1.623	3.48E-05	4.99E-01	2400	1.81	2.95E-02	1.23E-05	2.14E-05	4.13E-06	4.32E-06	1.88E-02	70.800
salic xx	3.54E-04	1.222	2.29E-05	3.76E-01	2400	1.36	2.58E-02	1.08E-05	1.87E-05	4.75E-06	4.86E-06	1.59E-02	61.920
salic xx	2.50E-04	0.898	1.34E-05	2.76E-01	2400	1.00	2.06E-02	8.58E-06	1.50E-05	5.09E-06	5.09E-06	1.22E-02	49.440
salic xx	1.77E-04	0.640	6.97E-06	1.97E-01	2400	0.71	1.50E-02	6.25E-06	1.09E-05	5.09E-06	5.65E-06	9.68E-03	36.000
salic xx	1.25E-04	0.438	4.61E-06	1.35E-01	2400	0.49	1.45E-02	6.04E-06	1.05E-05	6.95E-06	6.97E-06	8.17E-03	34.800
salic xx	8.84E-05	0.284	2.07E-06	8.75E-02	2400	0.32	1.00E-02	4.17E-06	7.26E-06	6.99E-06	7.85E-06	5.97E-03	24.000
salic xx	6.25E-05	0.172	1.17E-06	5.29E-02	2400	0.19	9.35E-03	3.90E-06	6.79E-06	9.84E-06	1.15E-05	5.28E-03	22.440
salic xx	4.42E-05	0.094	6.50E-07	2.90E-02	2400	0.11	9.48E-03	3.95E-06	6.89E-06	1.53E-05	1.54E-05	3.89E-03	22.752
salic xx	3.13E-05	0.046	2.14E-07	1.40E-02	2400	0.05	6.46E-03	2.69E-06	4.69E-06	1.57E-05	1.60E-05	1.94E-03	15.504
salic xx	2.21E-05	0.019	6.80E-08	5.85E-03	2400	0.02	4.93E-03	2.05E-06	3.58E-06	1.65E-05	1.48E-05	7.51E-04	11.832
salic xx	1.56E-05	0.007	1.38E-08	2.22E-03	2400	0.01	2.64E-03	1.10E-06	1.92E-06	1.06E-05	8.51E-06	1.63E-04	6.336
salic xx	1.10E-05	0.003	1.52E-09	8.00E-04	2400	0.00	8.06E-04	3.36E-07	5.85E-07	3.53E-06	2.49E-06	1.73E-05	1.934
dense lithic	1.60E-02	13.785	3.13E-05	4.24E+00	2570	15.37	3.35E-03	1.30E-06	2.27E-06	5.30E-08	1.15E-07	4.54E-03	8.610
dense lithic	1.13E-02	11.191	1.01E-04	3.44E+00	2570	12.48	1.33E-02	5.18E-06	9.02E-06	2.59E-07	2.23E-07	7.16E-03	34.181
dense lithic	8.00E-03	9.061	3.57E-05	2.79E+00	2570	10.11	5.81E-03	2.26E-06	3.94E-06	1.40E-07	2.62E-07	6.80E-03	14.932
dense lithic	5.66E-03	7.318	9.13E-05	2.25E+00	2570	8.16	1.84E-02	7.16E-06	1.25E-05	5.47E-07	6.96E-07	1.46E-02	47.288
dense lithic	4.00E-03	5.897	1.13E-04	1.81E+00	2570	6.58	2.83E-02	1.10E-05	1.92E-05	1.04E-06	1.08E-06	1.82E-02	72.731
dense lithic	2.83E-03	4.741	8.20E-05	1.46E+00	2570	5.29	2.55E-02	9.92E-06	1.73E-05	1.17E-06	1.38E-06	1.87E-02	65.535
dense lithic	2.00E-03	3.805	8.52E-05	1.17E+00	2570	4.24	3.30E-02	1.28E-05	2.24E-05	1.87E-06	2.03E-06	2.22E-02	84.810
dense lithic	1.41E-03	3.045	7.00E-05	9.37E-01	2570	3.40	3.39E-02	1.32E-05	2.30E-05	2.40E-06	2.48E-06	2.17E-02	87.123
dense lithic	1.00E-03	2.424	4.98E-05	7.46E-01	2570	2.70	3.03E-02	1.18E-05	2.06E-05	2.68E-06	3.08E-06	2.14E-02	77.871
dense lithic	7.07E-04	1.912	4.66E-05	5.88E-01	2570	2.13	3.59E-02	1.40E-05	2.44E-05	4.01E-06	3.88E-06	2.13E-02	92.263

dense lithic	5.00E-04	1.488	2.54E-05	4.58E-01	2570	1.66	2.52E-02	9.81E-06	1.71E-05	3.59E-06	3.75E-06	1.60E-02	64.764
dense lithic	3.54E-04	1.135	1.72E-05	3.49E-01	2570	1.27	2.23E-02	8.68E-06	1.51E-05	4.12E-06	4.11E-06	1.34E-02	57.311
dense lithic	2.50E-04	0.846	9.59E-06	2.60E-01	2570	0.94	1.67E-02	6.50E-06	1.13E-05	4.08E-06	4.13E-06	1.00E-02	42.919
dense lithic	1.77E-04	0.613	5.37E-06	1.89E-01	2570	0.68	1.29E-02	5.02E-06	8.75E-06	4.25E-06	4.27E-06	7.50E-03	33.153
dense lithic	1.25E-04	0.428	2.72E-06	1.32E-01	2570	0.48	9.38E-03	3.65E-06	6.36E-06	4.29E-06	4.28E-06	5.24E-03	24.107
dense lithic	8.84E-05	0.283	1.25E-06	8.72E-02	2570	0.32	6.48E-03	2.52E-06	4.40E-06	4.25E-06	4.73E-06	3.84E-03	16.654
dense lithic	6.25E-05	0.175	7.17E-07	5.38E-02	2570	0.19	6.05E-03	2.35E-06	4.10E-06	5.87E-06	6.83E-06	3.42E-03	15.549
dense lithic	4.42E-05	0.097	4.06E-07	3.00E-02	2570	0.11	6.14E-03	2.39E-06	4.17E-06	9.06E-06	9.14E-06	2.55E-03	15.780
dense lithic	3.13E-05	0.047	1.34E-07	1.46E-02	2570	0.05	4.18E-03	1.63E-06	2.84E-06	9.32E-06	9.50E-06	1.29E-03	10.743
dense lithic	2.21E-05	0.020	4.28E-08	6.06E-03	2570	0.02	3.20E-03	1.25E-06	2.17E-06	9.92E-06	8.87E-06	5.01E-04	8.224
dense lithic	1.56E-05	0.007	8.58E-09	2.28E-03	2570	0.01	1.71E-03	6.65E-07	1.16E-06	6.42E-06	5.13E-06	1.09E-04	4.395
dense lithic	1.10E-05	0.003	9.51E-10	8.31E-04	2570	0.00	5.19E-04	2.02E-07	3.52E-07	2.12E-06	1.49E-06	1.15E-05	1.334
femic xx	2.00E-03	4.962	7.38E-07	1.53E+00	3280	5.53	2.80E-04	8.54E-08	1.49E-07	9.59E-09	1.65E-08	3.00E-04	0.918
femic xx	1.41E-03	4.005	1.64E-06	1.23E+00	3280	4.47	7.72E-04	2.35E-07	4.10E-07	3.27E-08	5.76E-08	8.45E-04	2.532
femic xx	1.00E-03	3.207	3.75E-06	9.86E-01	3280	3.58	2.20E-03	6.71E-07	1.17E-06	1.16E-07	2.21E-07	2.60E-03	7.216
femic xx	7.07E-04	2.532	9.46E-06	7.79E-01	3280	2.82	7.03E-03	2.14E-06	3.74E-06	4.67E-07	7.21E-07	6.68E-03	23.058
femic xx	5.00E-04	1.962	1.61E-05	6.03E-01	3280	2.19	1.54E-02	4.70E-06	8.19E-06	1.31E-06	1.53E-06	1.09E-02	50.512
femic xx	3.54E-04	1.487	1.43E-05	4.57E-01	3280	1.66	1.81E-02	5.52E-06	9.62E-06	2.02E-06	2.00E-06	1.09E-02	59.368
femic xx	2.50E-04	1.100	7.72E-06	3.39E-01	3280	1.23	1.32E-02	4.02E-06	7.02E-06	1.97E-06	1.77E-06	7.12E-03	43.296
femic xx	1.77E-04	0.792	2.70E-06	2.44E-01	3280	0.88	6.42E-03	1.96E-06	3.41E-06	1.31E-06	1.03E-06	2.99E-03	21.058
femic xx	1.25E-04	0.549	4.03E-07	1.69E-01	3280	0.61	1.38E-03	4.21E-07	7.33E-07	3.95E-07	3.96E-07	7.94E-04	4.526
femic xx	8.84E-05	0.363	1.84E-07	1.12E-01	3280	0.40	9.57E-04	2.92E-07	5.09E-07	3.97E-07	4.44E-07	5.89E-04	3.139
femic xx	6.25E-05	0.224	1.06E-07	6.90E-02	3280	0.25	8.88E-04	2.71E-07	4.72E-07	5.54E-07	6.48E-07	5.32E-04	2.913
femic xx	4.42E-05	0.127	6.09E-08	3.91E-02	3280	0.14	9.02E-04	2.75E-07	4.79E-07	8.69E-07	8.84E-07	4.11E-04	2.959
femic xx	3.13E-05	0.064	2.09E-08	1.97E-02	3280	0.07	6.15E-04	1.88E-07	3.27E-07	9.18E-07	9.51E-07	2.23E-04	2.017
femic xx	2.21E-05	0.028	7.00E-09	8.58E-03	3280	0.03	4.72E-04	1.44E-07	2.51E-07	1.03E-06	9.30E-07	9.48E-05	1.548
femic xx	1.56E-05	0.011	1.45E-09	3.32E-03	3280	0.01	2.53E-04	7.71E-08	1.34E-07	7.03E-07	5.62E-07	2.21E-05	0.830
femic xx	1.10E-05	0.004	1.56E-10	1.20E-03	3280	0.00	7.52E-05	2.29E-08	4.00E-08	2.35E-07	1.65E-07	2.38E-06	0.247

Summary of results	
0.593	Sr ($kgm^{-2}s^{-1}$)
1248.9	ρ_{dep} (kgm^{-3})
4.75E-04	A_r

	(ms^{-1})
1.5	d (m)
3159	t (s)

P_{navg}	1.950
P_{n*}	3.250

Supporting file E. Step-by-step calculation of the sedimentation rate S_r and deposition time t of the tractional layer with sand-wave bedforms cropping out at Sbirri. In yellow the main parametres. For symbols see the symbol list. $\gamma_i = \frac{c_{trans_i}}{\left(\left(10.065 * {}^{P}n_i/P_n^*\right) + 0.1579\right)}$; $\gamma_{true_i} = \gamma_i * 0.7 + \gamma_{i+1} * 0.3$.

u_* (ms^{-1})	0.43
ρ_s average (kgm^{-3})	2440
C_{tot} (-)	0.0006
ρ_{mix} (kgm^{-3})	1.835
τ (Pa)	0.343
D_{sm} (mm)	0.07
Re_* (-)	2
θ_t (-)	0.017
$\tau_{rsm}{}^*$ (-)	0.0128
τ_{rsm} (Pa)	0.1906
S_r (kgm^{-2}s^{-1})	0.096
ρ_{dep} (kgm^{-3})	1440
A_r (ms^{-1})	6.667E-05

Component	D_i (m)	D_i/D_{sm}	τ_{ri} (Pa)	τ/τ_{ri}	W_i^*	Q_{bi} (m^{2}s^{-1})	ϕ_i	ρ_{si} (kgm^{-3})
vesicular glass	5.66E-03	77.534	3.517	0.098	5.645E-08	4.665E-16	0.0013	596
vesicular glass	4.00E-03	54.795	2.787	0.123	1.608E-07	2.657E-15	0.0027	669
vesicular glass	2.83E-03	38.767	2.210	0.155	4.563E-07	6.034E-15	0.0021	751
vesicular glass	2.00E-03	27.397	1.752	0.196	1.300E-06	1.718E-14	0.0021	842
vesicular glass	1.41E-03	19.315	1.386	0.247	3.728E-06	1.048E-13	0.0045	945
vesicular glass	1.00E-03	13.699	1.101	0.311	1.051E-05	2.952E-13	0.0045	1060
vesicular glass	7.07E-04	9.685	0.872	0.393	2.994E-05	1.237E-12	0.0066	1189
vesicular glass	5.00E-04	6.849	0.688	0.499	8.729E-05	4.977E-12	0.0091	1334
vesicular glass	3.54E-04	4.849	0.530	0.647	2.827E-04	2.686E-11	0.0152	1497
vesicular glass	2.50E-04	3.425	0.392	0.876	1.101E-03	1.110E-10	0.0162	1679
vesicular glass	1.77E-04	2.425	0.292	1.176	4.151E-03	5.797E-10	0.0224	1884
vesicular glass	1.25E-04	1.712	0.233	1.474	3.471E-02	5.192E-09	0.0240	2114
vesicular glass	8.84E-05	1.211	0.201	1.703	7.723E-02	1.692E-08	0.0351	2372
vesicular glass	6.25E-05	0.856	0.184	1.864	1.169E-01	3.060E-08	0.0420	2560
vesicular glass	4.42E-05	0.605	0.173	1.983	1.504E-01	4.321E-08	0.0461	2560
vesicular glass	3.13E-05	0.429	0.165	2.079	1.799E-01	5.238E-08	0.0467	2560
vesicular glass	2.21E-05	0.303	0.158	2.166	2.083E-01	4.834E-08	0.0372	2560
vesicular glass	1.56E-05	0.214	0.152	2.250	2.371E-01	3.003E-08	0.0203	2560
vesicular glass	1.10E-05	0.151	0.147	2.336	2.676E-01	9.121E-09	0.0055	2560
salic xx	1.41E-03	19.315	1.386	0.247	3.728E-06	2.465E-14	0.0011	2400
salic xx	1.00E-03	13.699	1.101	0.311	1.051E-05	8.682E-14	0.0013	2400
salic xx	7.07E-04	9.685	0.872	0.393	2.994E-05	9.896E-13	0.0053	2400
salic xx	5.00E-04	6.849	0.688	0.499	8.729E-05	5.698E-12	0.0105	2400
salic xx	3.54E-04	4.849	0.530	0.647	2.827E-04	2.943E-11	0.0167	2400
salic xx	2.50E-04	3.425	0.392	0.876	1.101E-03	1.320E-10	0.0192	2400
salic xx	1.77E-04	2.425	0.292	1.176	4.151E-03	5.626E-10	0.0217	2400
salic xx	1.25E-04	1.712	0.233	1.474	3.471E-02	4.934E-09	0.0228	2400
salic xx	8.84E-05	1.211	0.201	1.703	7.723E-02	1.608E-08	0.0334	2400

salic xx	6.25E-05	0.856	0.184	1.864	1.169E-01	2.908E-08	0.0399	2400
salic xx	4.42E-05	0.605	0.173	1.983	1.504E-01	4.106E-08	0.0438	2400
salic xx	3.13E-05	0.429	0.165	2.079	1.799E-01	4.977E-08	0.0444	2400
salic xx	2.21E-05	0.303	0.158	2.166	2.083E-01	4.594E-08	0.0354	2400
salic xx	1.56E-05	0.214	0.152	2.250	2.371E-01	2.853E-08	0.0193	2400
salic xx	1.10E-05	0.151	0.147	2.336	2.676E-01	8.667E-09	0.0052	2400
dense lithic	2.83E-03	38.767	2.210	0.155	4.563E-07	5.279E-15	0.0019	2588
dense lithic	2.00E-03	27.397	1.752	0.196	1.300E-06	2.148E-14	0.0027	2588
dense lithic	1.41E-03	19.315	1.386	0.247	3.728E-06	8.011E-14	0.0034	2588
dense lithic	1.00E-03	13.699	1.101	0.311	1.051E-05	2.604E-13	0.0040	2588
dense lithic	7.07E-04	9.685	0.872	0.393	2.994E-05	2.919E-12	0.0156	2588
dense lithic	5.00E-04	6.849	0.688	0.499	8.729E-05	9.305E-12	0.0171	2588
dense lithic	3.54E-04	4.849	0.530	0.647	2.827E-04	3.971E-11	0.0225	2588
dense lithic	2.50E-04	3.425	0.392	0.876	1.101E-03	1.374E-10	0.0200	2588
dense lithic	1.77E-04	2.425	0.292	1.176	4.151E-03	5.797E-10	0.0224	2588
dense lithic	1.25E-04	1.712	0.233	1.474	3.471E-02	4.590E-09	0.0212	2588
dense lithic	8.84E-05	1.211	0.201	1.703	7.723E-02	1.495E-08	0.0310	2588
dense lithic	6.25E-05	0.856	0.184	1.864	1.169E-01	2.705E-08	0.0371	2588
dense lithic	4.42E-05	0.605	0.173	1.983	1.504E-01	3.819E-08	0.0407	2588
dense lithic	3.13E-05	0.429	0.165	2.079	1.799E-01	4.630E-08	0.0413	2588
dense lithic	2.21E-05	0.303	0.158	2.166	2.083E-01	4.273E-08	0.0329	2588
dense lithic	1.56E-05	0.214	0.152	2.250	2.371E-01	2.654E-08	0.0180	2588
dense lithic	1.10E-05	0.151	0.147	2.336	2.676E-01	8.062E-09	0.0048	2588
					Q_b (m^2s^{-1})	6.665E-07	1	

Supporting file F. Step-by-step calculation of the bedload transportation rate $Q_{b,}$ Sedimentation rate S_r and aggradation rate A_r of the fine-ash structureless layer at Camaldoli. In yellow the main parametres. For symbols see the symbol list.

Input data from Pyflow	
u^* (ms^{-1})	2.00
C_{tot}	0.00175
P_{nsusp}	0.861

Component	D_i (m)	P_{ni}	$P_{ni}{}^*C_{transi}$	$P_{ni}/P_n{}^*$	ρ_{si} (kgm^{-3})	w_t (ms^{-1})	ϕ_i	Vol. fraction (m^3kg^{-1})	C_{transi}	γ_i	γ_{truei}	S_{ri} ($kgm^{-2}s^{-1}$)	$\rho_{si}{}^*\phi_i$ (kgm^{-3})
vesicular glass	2.83E-03	4.484	9.51E-05	2.14	1508	3.015	7.62E-03	5.05E-06	2.12E-05	9.68E-07	1.58E-06	7.16E-03	11.49
vesicular glass	2.00E-03	3.831	1.45E-04	1.83	1615	2.576	1.46E-02	9.04E-06	3.79E-05	2.02E-06	2.65E-06	1.10E-02	23.58
vesicular glass	1.41E-03	3.194	2.05E-04	1.52	1723	2.148	2.64E-02	1.53E-05	6.43E-05	4.11E-06	5.14E-06	1.90E-02	45.48
vesicular glass	1.00E-03	2.613	2.53E-04	1.25	1830	1.757	4.22E-02	2.31E-05	9.68E-05	7.54E-06	7.99E-06	2.57E-02	77.23
vesicular glass	7.07E-04	2.102	1.97E-04	1.00	1937	1.414	4.32E-02	2.23E-05	9.36E-05	9.04E-06	1.00E-05	2.74E-02	83.70
vesicular glass	5.00E-04	1.664	1.69E-04	0.79	2045	1.119	4.94E-02	2.42E-05	1.01E-04	1.23E-05	1.26E-05	2.89E-02	101.02
vesicular glass	3.54E-04	1.293	1.11E-04	0.62	2152	0.870	4.39E-02	2.04E-05	8.56E-05	1.33E-05	1.29E-05	2.41E-02	94.49
vesicular glass	2.50E-04	1.292	9.88E-05	0.62	2260	0.869	4.12E-02	1.82E-05	7.65E-05	1.19E-05	1.19E-05	2.34E-02	93.10
vesicular glass	1.77E-04	0.996	5.91E-05	0.48	2367	0.670	3.35E-02	1.42E-05	5.94E-05	1.19E-05	1.27E-05	2.01E-02	79.30
vesicular glass	1.25E-04	0.677	3.39E-05	0.32	2475	0.456	2.95E-02	1.19E-05	5.00E-05	1.45E-05	1.67E-05	1.88E-02	73.00
vesicular glass	8.84E-05	0.433	2.13E-05	0.21	2582	0.291	3.03E-02	1.17E-05	4.92E-05	2.18E-05	2.09E-05	1.57E-02	78.24
vesicular glass	6.25E-05	0.257	6.73E-06	0.12	2690	0.173	1.68E-02	6.25E-06	2.62E-05	1.87E-05	2.05E-05	9.55E-03	45.18
vesicular glass	4.42E-05	0.140	2.92E-06	0.07	2797	0.094	1.39E-02	4.97E-06	2.09E-05	2.49E-05	2.55E-05	6.73E-03	38.88
vesicular glass	3.13E-05	0.066	8.55E-07	0.03	2760	0.045	8.51E-03	3.08E-06	1.29E-05	2.70E-05	2.87E-05	3.53E-03	23.49
vesicular glass	2.21E-05	0.028	2.74E-07	0.01	2760	0.019	6.35E-03	2.30E-06	9.65E-06	3.27E-05	3.11E-05	1.64E-03	17.53
vesicular glass	1.56E-05	0.011	6.03E-08	0.01	2760	0.007	3.78E-03	1.37E-06	5.75E-06	2.75E-05	2.30E-05	4.50E-04	10.43
vesicular glass	1.10E-05	0.003	6.39E-09	0.00	2760	0.002	1.40E-03	5.07E-07	2.13E-06	1.23E-05	8.64E-06	4.77E-05	3.86
femic xx	2.00E-03	6.344	1.10E-05	3.03	3280	4.267	1.35E-03	4.12E-07	1.73E-06	5.58E-08	1.16E-07	1.62E-03	4.43
femic xx	1.41E-03	5.206	2.64E-05	2.48	3280	3.501	3.96E-03	1.21E-06	5.07E-06	1.99E-07	2.20E-07	2.53E-03	12.99
femic xx	1.00E-03	4.166	2.29E-05	1.99	3280	2.802	4.29E-03	1.31E-06	5.49E-06	2.70E-07	3.57E-07	3.28E-03	14.07
femic xx	7.07E-04	3.270	2.93E-05	1.56	3280	2.199	7.01E-03	2.14E-06	8.97E-06	5.60E-07	7.04E-07	5.08E-03	22.99
femic xx	5.00E-04	2.527	3.26E-05	1.21	3280	1.699	1.01E-02	3.08E-06	1.29E-05	1.04E-06	1.18E-06	6.57E-03	33.13
femic xx	3.54E-04	1.920	2.73E-05	0.92	3280	1.291	1.11E-02	3.38E-06	1.42E-05	1.50E-06	1.69E-06	7.17E-03	36.41
femic xx	2.50E-04	1.428	2.17E-05	0.68	3280	0.961	1.19E-02	3.63E-06	1.52E-05	2.15E-06	2.16E-06	6.80E-03	39.03
femic xx	1.77E-04	1.322	1.89E-05	0.63	3280	0.889	1.12E-02	3.41E-06	1.43E-05	2.18E-06	2.09E-06	6.11E-03	36.74
femic xx	1.25E-04	0.898	7.67E-06	0.43	3280	0.604	6.68E-03	2.04E-06	8.55E-06	1.89E-06	2.22E-06	4.39E-03	21.91
femic xx	8.84E-05	0.577	5.06E-06	0.28	3280	0.388	6.86E-03	2.09E-06	8.78E-06	2.97E-06	2.87E-06	3.66E-03	22.50
femic xx	6.25E-05	0.347	1.69E-06	0.17	3280	0.233	3.81E-03	1.16E-06	4.87E-06	2.65E-06	2.96E-06	2.26E-03	12.50

femic xx	4.42E-05	0.193	7.78E-07	0.09	3280	0.130	3.15E-03	9.60E-07	4.03E-06	3.68E-06	3.73E-06	1.59E-03	10.33
femic xx	3.13E-05	0.100	2.46E-07	0.05	3280	0.067	1.93E-03	5.88E-07	2.47E-06	3.85E-06	4.12E-06	9.06E-04	6.33
femic xx	2.21E-05	0.048	8.89E-08	0.02	3280	0.032	1.45E-03	4.42E-07	1.86E-06	4.75E-06	4.60E-06	4.86E-04	4.76
femic xx	1.56E-05	0.021	2.34E-08	0.01	3280	0.014	8.64E-04	2.63E-07	1.11E-06	4.24E-06	3.56E-06	1.67E-04	2.83
femic xx	1.10E-05	0.008	3.28E-09	0.00	3280	0.006	3.05E-04	9.30E-08	3.90E-07	1.96E-06	1.38E-06	2.57E-05	1.00
dense lithic	5.66E-03	6.527	5.41E-05	3.11	2570	4.390	5.08E-03	1.98E-06	8.29E-06	2.61E-07	3.45E-07	3.90E-03	13.06
dense lithic	4.00E-03	5.730	4.52E-05	2.73	2570	3.853	4.83E-03	1.88E-06	7.89E-06	2.82E-07	3.90E-07	3.86E-03	12.41
dense lithic	2.83E-03	4.904	7.53E-05	2.34	2570	3.298	9.40E-03	3.66E-06	1.53E-05	6.41E-07	1.11E-06	9.45E-03	24.16
dense lithic	2.00E-03	4.078	1.80E-04	1.95	2570	2.743	2.71E-02	1.05E-05	4.42E-05	2.22E-06	3.01E-06	2.12E-02	69.65
dense lithic	1.41E-03	3.307	2.61E-04	1.58	2570	2.224	4.83E-02	1.88E-05	7.89E-05	4.87E-06	5.60E-06	3.20E-02	124.13
dense lithic	1.00E-03	2.630	2.48E-04	1.26	2570	1.769	5.78E-02	2.25E-05	9.44E-05	7.31E-06	7.82E-06	3.55E-02	148.55
dense lithic	7.07E-04	2.059	1.88E-04	0.98	2570	1.385	5.60E-02	2.18E-05	9.14E-05	9.01E-06	9.57E-06	3.41E-02	143.92
dense lithic	5.00E-04	1.587	1.35E-04	0.76	2570	1.067	5.23E-02	2.04E-05	8.54E-05	1.09E-05	1.08E-05	2.96E-02	134.41
dense lithic	3.54E-04	1.200	7.62E-05	0.57	2570	0.807	3.89E-02	1.51E-05	6.35E-05	1.06E-05	9.98E-06	2.07E-02	99.97
dense lithic	2.50E-04	1.277	6.86E-05	0.61	2570	0.859	3.29E-02	1.28E-05	5.37E-05	8.46E-06	8.43E-06	1.86E-02	84.55
dense lithic	1.77E-04	0.974	3.97E-05	0.46	2570	0.655	2.50E-02	9.73E-06	4.08E-05	8.36E-06	9.09E-06	1.53E-02	64.25
dense lithic	1.25E-04	0.628	2.17E-05	0.30	2570	0.423	2.12E-02	8.25E-06	3.46E-05	1.08E-05	1.30E-05	1.41E-02	54.48
dense lithic	8.84E-05	0.375	1.34E-05	0.18	2570	0.253	2.18E-02	8.48E-06	3.56E-05	1.80E-05	1.78E-05	1.15E-02	56.03
dense lithic	6.25E-05	0.204	4.02E-06	0.10	2570	0.137	1.21E-02	4.71E-06	1.98E-05	1.72E-05	1.98E-05	6.96E-03	31.10
dense lithic	4.42E-05	0.098	1.61E-06	0.05	2570	0.066	1.00E-02	3.89E-06	1.63E-05	2.57E-05	2.64E-05	4.49E-03	25.70
dense lithic	3.13E-05	0.041	4.13E-07	0.02	2570	0.028	6.12E-03	2.38E-06	9.99E-06	2.79E-05	2.94E-05	2.10E-03	15.73
dense lithic	2.21E-05	0.014	1.06E-07	0.01	2570	0.010	4.57E-03	1.78E-06	7.46E-06	3.29E-05	3.07E-05	7.50E-04	11.74
dense lithic	1.56E-05	0.003	1.38E-08	0.00	2570	0.002	2.72E-03	1.06E-06	4.44E-06	2.57E-05	2.02E-05	1.09E-04	6.99
dense lithic	1.10E-05	0.013	2.06E-08	0.01	2570	0.009	9.91E-04	3.86E-07	1.62E-06	7.37E-06	5.16E-06	1.13E-04	2.55
salic xx	2.00E-03	5.666	2.01E-06	2.70	2400	3.811	2.03E-04	8.46E-08	3.55E-07	1.28E-08	4.42E-08	4.05E-04	0.49
salic xx	1.41E-03	4.616	1.09E-05	2.20	2400	3.104	1.35E-03	5.63E-07	2.36E-06	1.05E-07	1.35E-07	1.01E-03	3.24
salic xx	1.00E-03	3.672	1.37E-05	1.75	2400	2.469	2.13E-03	8.88E-07	3.72E-06	2.07E-07	2.77E-07	1.64E-03	5.11
salic xx	7.07E-04	2.868	1.77E-05	1.37	2400	1.929	3.53E-03	1.47E-06	6.17E-06	4.39E-07	5.27E-07	2.44E-03	8.47
salic xx	5.00E-04	2.205	1.75E-05	1.05	2400	1.483	4.55E-03	1.90E-06	7.96E-06	7.33E-07	1.01E-06	3.61E-03	10.92
salic xx	3.54E-04	1.665	2.29E-05	0.79	2400	1.120	7.87E-03	3.28E-06	1.38E-05	1.67E-06	1.83E-06	4.93E-03	18.89

salic xx	2.50E-04	1.277	1.79E-05	0.61	2400	0.859	8.03E-03	3.35E-06	1.40E-05	2.21E-06	2.46E-06	5.06E-03	19.27
salic xx	1.77E-04	1.087	1.79E-05	0.52	2400	0.731	9.40E-03	3.92E-06	1.64E-05	3.03E-06	3.16E-06	5.54E-03	22.56
salic xx	1.25E-04	0.731	9.38E-06	0.35	2400	0.492	7.34E-03	3.06E-06	1.28E-05	3.46E-06	4.07E-06	4.80E-03	17.62
salic xx	8.84E-05	0.465	6.13E-06	0.22	2400	0.312	7.54E-03	3.14E-06	1.32E-05	5.47E-06	5.29E-06	3.97E-03	18.10
salic xx	6.25E-05	0.276	2.01E-06	0.13	2400	0.186	4.17E-03	1.74E-06	7.29E-06	4.87E-06	5.43E-06	2.42E-03	10.01
salic xx	4.42E-05	0.153	9.21E-07	0.07	2400	0.103	3.45E-03	1.44E-06	6.03E-06	6.72E-06	6.75E-06	1.66E-03	8.28
salic xx	3.13E-05	0.079	2.91E-07	0.04	2400	0.053	2.11E-03	8.79E-07	3.69E-06	6.83E-06	7.18E-06	9.14E-04	5.06
salic xx	2.21E-05	0.038	1.05E-07	0.02	2400	0.026	1.57E-03	6.54E-07	2.75E-06	8.01E-06	7.65E-06	4.70E-04	3.77
salic xx	1.56E-05	0.017	2.83E-08	0.01	2400	0.012	9.40E-04	3.92E-07	1.64E-06	6.81E-06	5.74E-06	1.58E-04	2.26
salic xx	1.10E-05	0.007	4.42E-09	0.00	2400	0.005	3.56E-04	1.48E-07	6.22E-07	3.24E-06	2.27E-06	2.56E-05	0.85

Summary of results	
0.589	Sr ($kgm^{-2}s^{-1}$)
1476	ρ_{dep} (kgm^{-3})
0.00040	A_r (ms^{-1})
0.15	d (m)
375.7	t (s)

P_{navg}	1.80E+00
P_{n*}	2.10E+00

Supporting file G. Step-by-step calculation of the sedimentation rate S_r of the tractive layer cropping under the massive bed at the "split location". In yellow the main parametres. For symbols see the symbol list. $\gamma_i = \frac{c_{trans_i}}{\left(\left(10.065 * {}^{P}n_i/P_n^*\right) + 0.1579\right)}$; $\gamma_{true_i} = \gamma_i * 0.7 + \gamma_{i+1} * 0.3$.